# Indefinite and bidirectional near-infrared nanocrystal photoswitching

https://doi.org/10.1038/s41586-023-06076-7

Received: 5 August 2022

Accepted: 12 April 2023

Published online: 31 May 2023



Check for updates

Changhwan Lee<sup>1</sup>, Emma Z. Xu<sup>1</sup>, Kevin W. C. Kwock<sup>2</sup>, Ayelet Teitelboim<sup>3</sup>, Yawei Liu<sup>3,4</sup>, Hye Sun Park<sup>5</sup>, Benedikt Ursprung<sup>1</sup>, Mark E. Ziffer<sup>6</sup>, Yuzuka Karube<sup>7</sup>, Natalie Fardian-Melamed<sup>1</sup>, Cassio C. S. Pedroso<sup>3</sup>, Jongwoo Kim<sup>8</sup>, Stefanie D. Pritzl<sup>9,10</sup>, Sang Hwan Nam<sup>8</sup>, Theobald Lohmueller<sup>9</sup>, Jonathan S. Owen<sup>7</sup>, Peter Ercius<sup>3</sup>, Yung Doug Suh<sup>8,11,12,13,⊠</sup>, Bruce E. Cohen<sup>3,14,⊠</sup>, Emory M. Chan<sup>3,⊠</sup> & P. James Schuck<sup>1,⊠</sup>

Materials whose luminescence can be switched by optical stimulation drive technologies ranging from superresolution imaging<sup>1-4</sup>, nanophotonics<sup>5</sup>, and optical data storage<sup>6,7</sup>, to targeted pharmacology, optogenetics, and chemical reactivity<sup>8</sup>. These photoswitchable probes, including organic fluorophores and proteins, can be prone to photodegradation and often operate in the ultraviolet or visible spectral regions. Colloidal inorganic nanoparticles<sup>6,9</sup> can offer improved stability, but the ability to switch emission bidirectionally, particularly with near-infrared (NIR) light, has not, to our knowledge, been reported in such systems. Here, we present two-way, NIR photoswitching of avalanching nanoparticles (ANPs), showing full optical control of upconverted emission using phototriggers in the NIR-I and NIR-II spectral regions useful for subsurface imaging. Employing single-step photodarkening 10-13 and photobrightening<sup>12,14-16</sup>, we demonstrate indefinite photoswitching of individual nanoparticles (more than 1,000 cycles over 7 h) in ambient or aqueous conditions without measurable photodegradation. Critical steps of the photoswitching mechanism are elucidated by modelling and by measuring the photon avalanche properties of single ANPs in both bright and dark states. Unlimited, reversible photoswitching of ANPs enables indefinitely rewritable two-dimensional and three-dimensional multilevel optical patterning of ANPs, as well as optical nanoscopy with sub-Å localization superresolution that allows us to distinguish individual ANPs within tightly packed clusters.

Upconverting nanoparticles (UCNPs) are lanthanide ion (Ln<sup>3+</sup>)-based phosphors that efficiently convert near-infrared (NIR) light to higher energies in the NIR, visible or ultraviolet (UV) regions 17-20. Unlike  $organic ^{4,21-25}, protein ^{24,26,27} \ or \ hybrid \ organic -inorganic \ luminescent$ probes<sup>28</sup>, UCNPs do not measurably photobleach, even with extended single-particle excitation under ambient conditions<sup>17,29-31</sup> or within microlasers under high pump powers<sup>32,33</sup>. While this exceptional photostability suggests that Ln3+-based UCNPs cannot be modulated by light, certain Ln<sup>3+</sup>-based bulk materials have been reported to be susceptible to photodarkening or brightening 11,34-37. Based on observations of photodarkening in Tm<sup>3+</sup>-doped fibres<sup>11,35,37</sup> and studies of colour centres and charge traps in UCNPs<sup>15,16,38,39</sup>, we sought to determine whether Tm3+-doped avalanching nanoparticles (ANPs) can be modulated by light in the same manner. ANPs are UCNPs with the steepest nonlinear emission response of any nanoscale material 20,40,41, which is enabled by the photon avalanching (PA) upconversion mechanism. Single-ANP characterization has shown that relatively minor variations in shell thickness lead to sharp changes in avalanche threshold<sup>42</sup>. This suggests that light-induced charge or energy transfer within the nanocrystal might also shift the PA threshold, magnifying the influence of a minute density of trap states into major emission differences (Fig. 1a,b).

To determine whether ANPs are capable of photoswitching, we characterized single, core-shell NaYF<sub>4</sub> ANPs with 8 mol% Tm<sup>3+</sup> under 1,064-nm excitation at a range of power densities (Extended Data Fig. 1). Tm<sup>3+</sup>-doped ANPs were grown as reported<sup>43-45</sup> and Gd<sup>3+</sup> was added to the shells of some batches of ANPs to facilitate hexagonal shell growth 46 (Supplementary Figs. 1 and 2 and Supplementary Tables 1 and 2). By advanced scanning transmission electron microscopy (STEM) imaging

Department of Mechanical Engineering, Columbia University, New York, NY, USA, 2Department of Electrical Engineering, Columbia University, New York, NY, USA, 3The Molecular Foundry, Lawrence Berkeley National Laboratory, Berkeley, CA, USA, 4State Key Laboratory of Rare Earth Resource Utilization, Changehun Institute of Applied Chemistry, Chinese Academy of Sciences, Changchun, China. Fresearch Center for Bioconvergence Analysis, Korea Basic Science Institute (KBSI), Cheongju, South Korea. Department of Physics, Columbia University, New York, NY, USA, Department of Chemistry, Columbia University, New York, NY, USA, Laboratory for Advanced Molecular Probing (LAMP), Korea Research Institute of Chemical Technology (KRICT), Daejeon, South Korea. 9Chair for Photonics and Optoelectronics, Nano-Institute Munich, Ludwig-Maximilians Universität München, Munich, Germany. 10 Department of Physics and Debye Institute for Nanomaterials Science, Utrecht University, Utrecht, The Netherlands. 1Department of Chemistry, Ulsan National Institute of Science and Technology (UNIST), Ulsan, South Korea. <sup>12</sup>School of Energy and Chemical Engineering, Ulsan National Institute of Science and Technology (UNIST), Ulsan, South Korea. <sup>13</sup>Center for Multidimensional Carbon Materials (CMCM), Institute for Basic Science (IBS), Ulsan, South Korea. 14 Division of Molecular Biophysics and Integrated Bioimaging, Lawrence Berkeley National Laboratory, Berkeley, CA, USA. Se-mail: ydsuh@ unist.ac.kr; becohen@lbl.gov; emchan@lbl.gov; p.i.schuck@columbia.edu

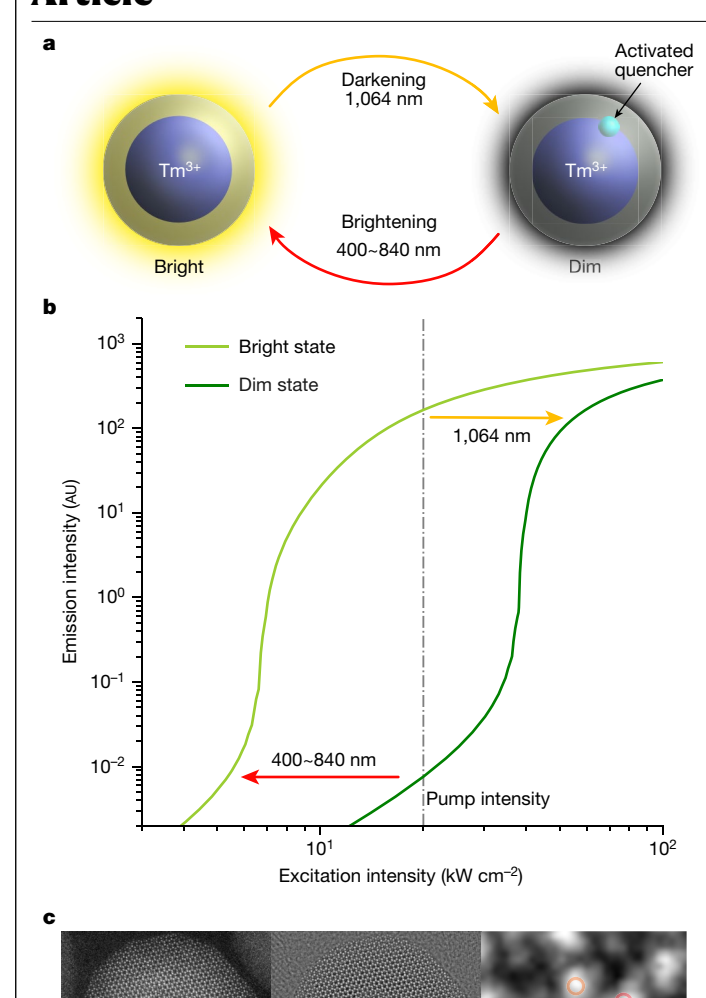


**Fig. 1**| **Photoswitchable PA nanoparticles. a**, Schematic highlighting the fully reversible NIR photoswitching response of ANPs. Emission is photodarkened using 1,064 nm light and photobrightened using wavelengths between 400 nm and 840 nm. **b**, Optical manipulation of the PA threshold in ANPs enables photoswitching behaviour. The plots are derived from the differential rate equation fits of experimental data in Fig. 3a. **c**, High-angle annular dark-field

STEM (left), differential phase contrast-STEM (middle) and magnified

positions are 50% Na/50% Y (red circle); Y (orange); F (green); Na (blue).

differential phase contrast-STEM overlaid with NaYF<sub>4</sub> unit cell (right) ANP

images. Scale bars in c, 4 nm (left and middle); 2 Å (right). NaYF<sub>4</sub> crystallographic

(Fig.1c), these ANPs are pure  $\beta$ -NaYF<sub>4</sub> without any observable extended defects or a clear core–shell interface. Above the avalanching threshold intensity  $I_{th}$ , the ANPs exhibit extremely nonlinear luminescence at 800 nm. As the pump intensity is increased well above  $I_{th}$  (Extended Data Fig. 1c,d), we observe that single ANPs darken or blink, exhibiting discontinuous, single-step jumps in luminescence (Extended Data Fig. 1c–e and Supplementary Figs. 3–9) within the time-resolution of our measurement (Supplementary Fig. 9 and Methods).

Additional measurements in ensemble films of 4% and 8% Tm<sup>3+</sup> nanocrystals suggest that PA plays a central role in the photodarkening. UCNPs doped with approximately 4% Tm<sup>3+</sup>, whose nonlinear emission is subavalanching (that is, energy looping<sup>43</sup>), do not show the same photodarkening or blinking behaviour (Extended Data Fig. 2a). When

doping is increased to  $8\% \, \text{Tm}^{3+}$ , the NPs exhibit pronounced PA and noticeable photodarkening at excitation intensities greater than or equal to  $143 \, \text{kW} \, \text{cm}^{-2}$  (approximately  $6 \, \times I_{\text{th}}$ , Extended Data Fig. 2b). We further observe that the rate of photodarkening accelerates as pump intensity increases. The ANP photodarkening is observed in particles with both thin (2.6 nm) and thick (8.5 nm) inert shells (Extended Data Fig. 3) as well as in ANPs in which passivating oleic acid ligands have been removed, which suggests that surface quenching does not play a major role. We also note that this dependence of photodarkening on Ln³+ content and pump intensity is consistent with the reported behaviours of Tm³+-doped fibres under intense 1,064 nm or 1,120 nm excitation  $^{11,35,37}$ .

To determine whether ANP photodarkening can be reversed, we examined the emission of 112 individual ANPs under various pump conditions (Fig. 2). Illuminating these photodarkened 8% Tm<sup>3+</sup> ANPs with 400 nm light results in full recovery of ANP brightness in all 112 ANPs. Further single-particle experiments (*vide infra*) have shown that this recovery is consistent for all ANPs examined, including those synthesized by different protocols (Supplementary Methods).

We then examined the nonlinear emission of single ANPs in both bright and photodarkened states to better understand the origins of these ANP behaviours. Photodarkened nanocrystals continue to exhibit PA emission, but with avalanching threshold intensities  $I_{\rm th}$  shifted to approximately five-fold higher pump intensities (Fig. 3a). Because of the steeply nonlinear PA process, the luminescence intensity at the same 1,064 nm pump intensity is reduced by greater than four orders of magnitude following this five-fold increase in  $I_{\rm th}$  (Extended Data Fig. 4a)  $^{20}$ . In this case, a saturating pumping intensity at first leads to bright ANP luminescence, but then shifts to weak pre-avalanche luminescence upon the attendant  $I_{\rm th}$  shift (Fig. 3a and Supplementary Fig. 10).

To further explain this, we fit the experimental power-dependent emission curves for darkened and undarkened ANPs to a rate equation model that we developed (Supplementary Methods and Supplementary Table 3) to describe the population balance and the radiative and non-radiative relaxation processes in ANPs<sup>20</sup> (Fig. 3a, dashed lines). Fits to the model reveal that, compared with undarkened ANPs, the darkened ANPs have a 5.3-fold faster overall relaxation rate ( $W_2$ ) from the  $^3F_4$  first excited state of Tm<sup>3+</sup> (Supplementary Information), consistent with the observed  $I_{\rm th}$  shift. This suggests an added, faster, loss of energy from  $^3F_4$ , which can be probed independently with luminescence lifetime measurements (see below).

To determine the dependence of luminescence recovery on illumination wavelength, we performed photobrightening scans from 400 nm to 940 nm on photodarkened ANP films (Fig. 3b, Extended Data Fig. 5 and Methods). Plots of luminescence recovery as functions of photobrightening wavelength (that is, photobrightening activity spectra) show a 5-100% recovery, depending on illumination wavelength. These photobrightening activity spectra (Fig. 3b and Extended Data Fig. 5a) include broad features at wavelengths less than 530 nm attributable to colour centres, and peaks at both 800 nm and 700 nm, which correspond directly to Tm<sup>3+3</sup>H<sub>4</sub> and <sup>3</sup>F<sub>2,3</sub> transitions. There is a sharp dip in the activity spectrum at 450 nm, where absorbed photons result in enhanced upconversion to photodarkening UV manifolds (Extended Data Fig. 6d). Higher resolution activity spectra reveal that the dip has a full-width at half-maximum (FWHM) of approximately 5 nm and luminescence studies show that UV emission is strongest under 450 nm excitation (which is resonant with excited-state Tm3+ absorptions), while no UV is observed under 480 nm excitation (corresponding to the <sup>3</sup>H<sub>6</sub>-to-<sup>1</sup>G<sub>4</sub> ground state absorption) (Extended Data Fig. 6c,d). Increasing the irradiation intensity or exposure time also enhances photobrightening, so that nearly full luminescence recovery can be achieved in a few seconds with 700 nm light (Fig. 3c).

To further elucidate the mechanisms of ANP photoswitching, we measured photobrightening efficiency in different ANP compositions. We observe that photobrightening efficiency increases as ANP

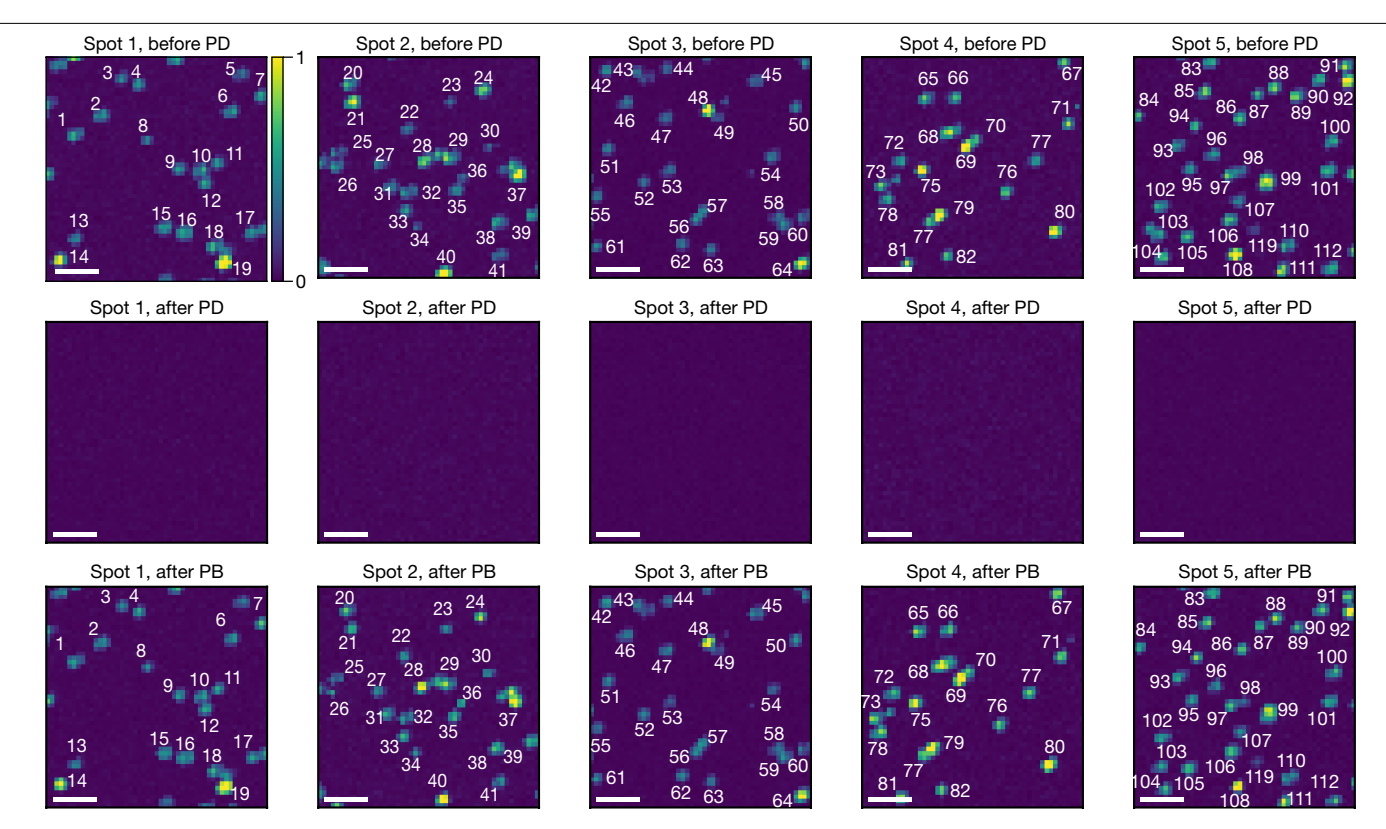


Fig. 2 | Consistent photoswitching of single ANPs. Single-particle imaging of ANPs before photodarkening (top), after photodarkening (middle) and after photobrightening (bottom) of 112 nanoparticles (mostly single ANPs, with a few dimers or small clusters). Columns are different regions of the sample. The

imaging and photodarkening (PD) intensities (1,064 nm) of 8% Tm<sup>3+</sup>17.4/2.6 nm core-shell ANPs are 28 kW cm<sup>-2</sup> and 140 kW cm<sup>-2</sup>, respectively. Photobrightening (PB) is achieved with 400 nm irradiation at 25 kW cm<sup>-2</sup>. Photoswitching is observed in all 112 ANPs.

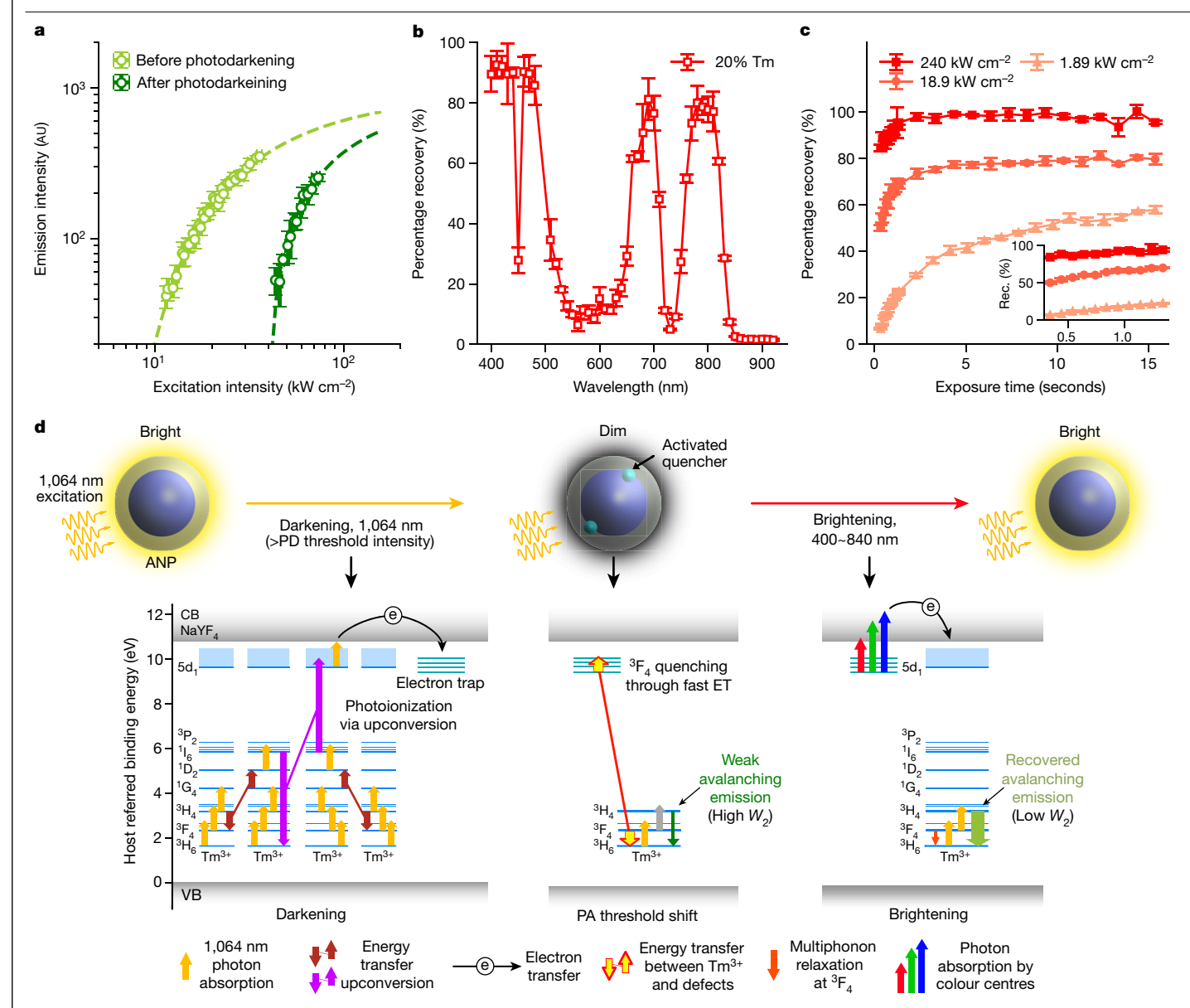
core diameters decrease (Extended Data Fig. 5b), which suggests that the number of active colour centres is determined by core volume or surface area. For 700 nm or 800 nm irradiation wavelengths, which correspond to Tm<sup>3+</sup> transitions, photobrightening becomes more efficient as Tm<sup>3+</sup> content increases from 8% to 30% (Extended Data Fig. 5c), which suggests that these wavelengths induce photobrightening by undergoing efficient upconversion to visible wavelengths (as higher ANP Tm<sup>3+</sup> content leads to shorter interionic distances, which increases the probability of upconversion), which then releases carriers trapped in the colour centres.

Taken together, these experiments and models are consistent with a photodarkening scheme in which extended ANP photoexcitation populates high-lying Tm<sup>3+</sup> excited states (for example, <sup>1</sup>I<sub>6</sub> and 5d<sup>1</sup>4f<sup>11</sup> states; as in Extended Data Figs. 6d and 7a) and ultimately results in the transfer of an electron (hole) from the Tm<sup>3+</sup> ion or the neighbouring atoms to the NaYF<sub>4</sub> conduction (valence) band (Fig. 3d and Extended Data Fig. 7b). These are then trapped in defects, activating colour centres that can quench the Tm<sup>3+3</sup>F<sub>4</sub>-to-ground-state transition. Direct evidence of such non-radiative quenching is provided by the decrease in the lifetime of this <sup>3</sup>F<sub>4</sub> state upon photodarkening (Extended Data Fig. 4b). Measurements of purely thermal luminescence recovery in photodarkened ANPs (Extended Data Fig. 7c) are consistent with trap depth energies suggested by the photobrightening activity spectra (Fig. 3b and Extended Data Fig. 5a). Because the process is fully reversible (Figs. 2 and 4 and vide infra) and does not involve surface quenching, any active colour centres are in the ANP interior, probably at the core-shell interface<sup>38</sup>. These interfacial point defects can arise during synthesis but are too minor to be imaged within the nanoparticle interior, even by high-resolution transmission electron microscopy (TEM) (Fig. 1c). As reported previously, such colour centres can have excited states that are capable of quenching the approximate 0.7 eV

 ${}^{3}F_{4}$  transition of Tm $^{3+}$  via energy transfer $^{15,16,38,47}$ , which increase  $W_{2}$ (Extended Data Fig. 4b) and, critically, shift  $I_{th}$  as observed (Figs. 1b) and 3a, Supplementary Fig. 10 and Supplementary Methods). Several photoionization mechanisms in Tm<sup>3+</sup>-doped glass fibres under NIR excitation have been proposed 10,35,37 and detailed identification of all transitions involved in the current system will require further in-depth study and development of more sensitive characterization tools, as current STEM imaging cannot observe interfacial point defects or dopants due to the projection through the entire structure along the beam direction.

We further investigated ANP photoswitching behaviour by measuring the emission of single aqueous 8% Tm<sup>3+</sup> core-shell ANPs <sup>48</sup> while sequentially exposing them to repeated cycles of 1,064 nm photodarkening followed by 700 nm photobrightening in ambient (Fig. 4a,c) or aqueous environments (Extended Data Fig. 8). Successful photoswitching of a single ANP was observed over 1,158 cycles in either ambient or aqueous conditions without any permanent photodegradation (Fig. 4c and Extended Data Fig. 8c). A probability histogram of single-ANP photoswitching shows that emission intensities overwhelmingly return to their original values (Fig. 4b). Partial emission recovery is occasionally observed (for example, cycle 1,152 in Fig. 4c), possibly originating from the involvement of additional trap or defect states 15,16,38,47. We observe no effect on photoswitching in ANPs with shell Gd3+, added to facilitate  $homogeneous\, shell\, growth^{46}, compared\, with\, those\, without\, (Fig.\, 5\, and\, 10\, cm)$ Extended Data Figs. 3 and 5).

Recent work has stressed the benefits of nanomaterials and photoswitchable emitters for optical data storage<sup>6,49,50</sup>. To determine whether ANP photoswitching can be leveraged in high-density patterning applications<sup>49</sup>, we deposited a thick (5 μm) film of 8% Tm<sup>3+</sup> ANPs onto a glass slide to darken and brighten in sequential two- and three-dimensional (2D and 3D) patterns, which were then imaged by



 $\label{eq:Fig. 3} \ | \ ANP\ photobrightening\ and\ photodarkening.\ a,\ Emission\ intensity\ (800\ nm)\ versus\ excitation\ intensity\ (1,064\ nm)\ of\ a\ single\ 8\%\ Tm^{3*}\ 17.3/5.6\ nm\ (core\ diameter-shell\ thickness)\ ANP\ before\ and\ after\ photodarkening.\ Switching\ between\ bright\ and\ dim\ states\ in\ ANPs\ is\ induced\ by\ shifting\ of\ the\ PA\ threshold,\ using\ 1,064\ nm\ light\ to\ darken\ and\ wavelengths\ less\ than\ or\ equal\ to\ 840\ nm\ to\ brighten.\ b,c,\ Photobrightening\ recovery\ of\ a\ photodarkened\ 20\%\ Tm^{3*}\ 10.4/2.7\ nm\ core-shell\ ANP\ ensemble\ film\ sample\ versus\ irradiation\ wavelength\ (b)\ or\ exposure\ time\ (c)\ .$  The\ photobrightening\ laser\ power\ at\ the\ sample\ is\ set\ to\ 1\ mW\ for\ all\ wavelengths\ in\ b,\ which\ corresponds\ to\ 90\ kW\ cm^{-2}

at 700 nm. Photobrightening exposure times are 1.3 s in **b**. Photodarkening exposure times are 1.2 s in **b** and **c**. 1,064-nm laser intensities for luminescence pumping and photodarkening are 69 kW cm<sup>-2</sup> and 345 kW cm<sup>-2</sup>, respectively, in **b** and **c**. For photobrightening, 700-nm irradiation intensities are shown in the legend in **c**. The inset in **c** is a magnified plot in the exposure-time range from 340 ms to 1,340 ms. Error bars are standard deviations of data points measured at four different spots in the same ensemble sample. **d**, Potential mechanistic pathways for photodarkening and photobrightening in ANPs. CB, conduction band; VB, valence band;  $W_{2}$ ,  ${}^{3}F_{4}$  relaxation rate.

confocal microscopy (Fig. 4d,e). Rewritable 2D patterns (Fig. 4d) were created using continuous-wave 1,064 nm and 700 nm focused beams for imaging/darkening and writing, respectively. The large nonlinearity of PA emission and photodarkening enables patterning resolutions less than 70 nm (ref. 20), with potential for exceptionally long storage lifetimes and unlimited read—write cycles due to ANP photostability (Fig. 4c and Extended Data Fig. 8c). Because the low scattering of NIR wavelengths in this process enables subsurface imaging into samples  $^{43,44}$ , we attempted optical patterning of a complex 3D design 3  $\mu$ m across in all three dimensions (Fig. 4e). This patterned diamond spiral shows voxel-to-voxel addressability that expands rewritable functionality beyond the existing thermal reset approach  $^{51}$ . Furthermore, multiple

grayscale levels of 800 nm Tm<sup>3+</sup> emission can be achieved in an ANP film using varying darkening wavelengths and photon doses, so that a single voxel can host five or more levels (Fig. 4f), expanding density by enabling multibit storage per voxel. These results highlight unique advantages offered by ANPs, including the combination of ideal photostability, extreme nonlinearity, sub-100 nm pixel sizes<sup>20</sup> and the use of NIR wavelengths for all read-write-reset processes.

To determine how indefinite ANP photoswitching affects localization accuracies in superresolution microscopy techniques, we used indefinite NIR PA localization microscopy (INPALM) to image single ANPs (Fig. 5a-e) and ANP clusters (Fig. 5d,e, Extended Data Fig. 9 and Methods). In related single-molecule localization microscopy

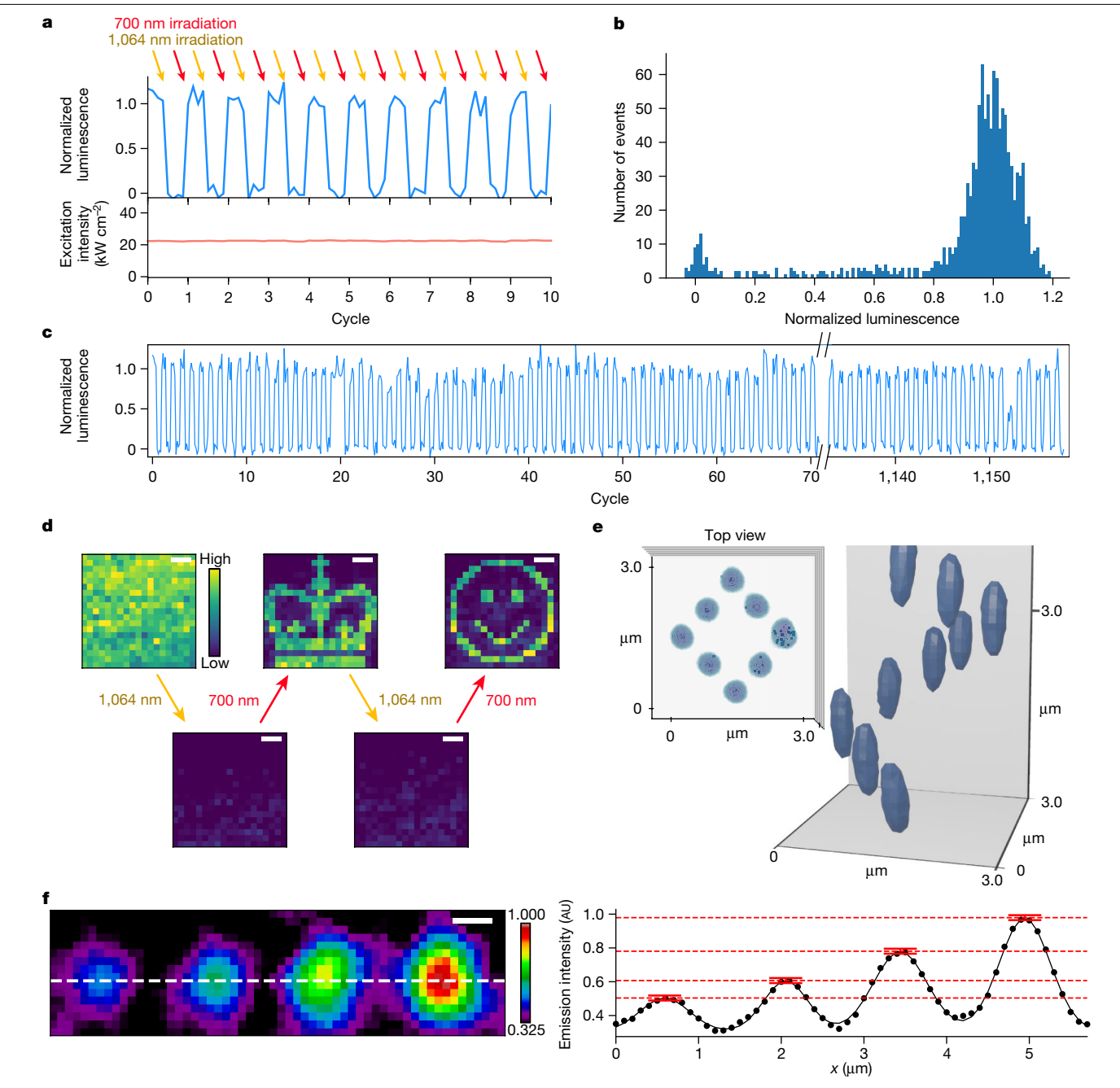


Fig. 4 | 2D and 3D microscale optical write, erase and rewrite of stable NIR-photoswitchable ANPs. a, Time-resolved luminescence and excitation  $intensities for a single \, aqueous \, 17.3/5.6 \, nm \, core-shell \, ANP \, under \, ambient$ conditions. A 1,064 nm pump intensity of 22.8 kW cm<sup>-2</sup> is continuously applied, which excites detectable emission in the bright state but not in the dim state. Irradiation conditions for darkening are 75.5 kW cm<sup>-2</sup> at 1,064 nm and 5 s (yellow arrows); and for photobrightening are 164.0 kW cm<sup>-2</sup> at 700 nm for 10 s (red arrows).  ${m b}$ , A histogram of the average emission intensity of the brightened ANP for 1,158 irradiation cycles. c, Trace of emission from the single aqueous ANP for the first 70 and last 25 irradiation cycles. d, Rewritable photopatterning of successive crown and face designs in a 100-nm-thick ANP film. The applicable

pixels in the sample were irradiated with intensity of 435 kW cm<sup>-2</sup> at 1,064 nm for 7 s for erasing and 164 kW cm<sup>-2</sup> at 700 nm for 5 s for positive lithography. Scale bars,  $5 \, \mu m$ . Colour bar, normalized luminescence intensity.  $\boldsymbol{e}$ , Side and top views of a 3D rendered image of a diamond spiral optically patterned into an approximately 5-µm-thick ANP film. The dark voxels in e represent emission intensity reduced by more than 70% relative to average emission intensity before photodarkening.  $\mathbf{f}$ , Left, an image of spots in a photodarkened  $8\% \, \mathrm{Tm}^{3+}$ ANP film photobrightened with increasing intensities of a 700 nm focused beam. Right, a linecut from the white dashed line. Scale bar, 500 nm. Colour bar, normalized luminescence intensity. Red dashed lines and red error bars are the amplitudes and standard deviations of fitted Gaussian curves, respectively.

methods<sup>1</sup>, accuracies are generally limited by the number of photons collected from a photoactivated probe before photobleaching<sup>1</sup>. As with photoactivated localization microscopy (PALM)<sup>52</sup>, in INPALM, the number of emitting ANPs is intentionally kept at low levels by choosing photobrightening illumination exposure times, intensities or wavelengths corresponding to small probabilities of luminescence recovery (Fig. 3b,c and Extended Data Figs. 5a and 7d). Because only a small subset of probes is emissive at a given time, non-overlapping point spread functions of emitted photons can be calculated to determine precise centroid fittings and localization accuracies. Unlike single-molecule localization microscopy methods where probes are irreversibly photobleached, ANPs may be brightened and darkened repeatedly and

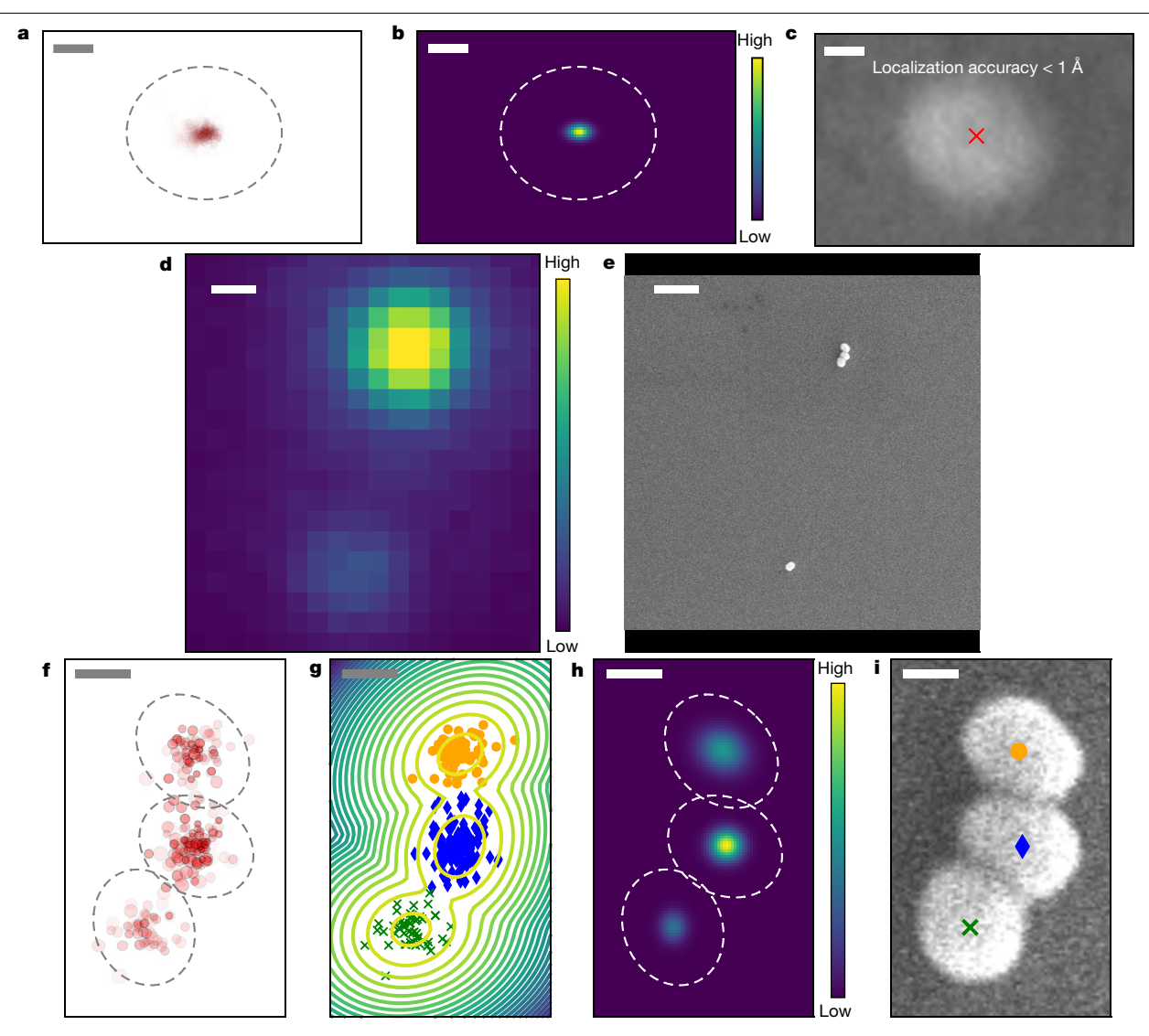


Fig. 5 | Indefinite NIR photon avalanching localization microscopy of ANPs. a, 2D map of the frame-by-frame localizations of a single 8% Tm $^{3+}$  core-inert NaYF $_4$  shell ANP (N = 403 frames; ANP is photoswitched off and on for each frame). See Methods for details of constructing this map. The red circle diameters correspond to the localization accuracy of each centroid. For each frame, the signal acquisition time is 1.8 s. b, Fitting of a 2D Gaussian function to the data in a. Colour bar in b: number of localizations in each pixel. c, The centroid, marked by a red  $\times$ , obtained from the 2D Gaussian fit in b, overlaid on an SEM image of the same ANP. Localization accuracy values (see text) include the contribution of 0.2 Å from drift correction. d.e, Confocal scanning image (d) and SEM image (e) of a single and a trimer of 8% Tm $^{3+}$  ANPs. Colour bar in

**d**, normalized luminescence intensity. **f**, Frame-by-frame localizations of the trimer in  $\mathbf{e}$  (N=172). For each frame, the signal acquisition time is 1.5 s. The red circle diameters correspond to the localization accuracy of each centroid. **g**, Clustering of localizations in **f** using the Gaussian mixture method (Methods). **h**, fitting of 2D Gaussians to the clustered localizations in **g**. Colour bar, number of localizations in each pixel. **i**, The centroids derived from the 2D Gaussian fits overlaid on an SEM image of the trimer. Localization accuracies (symbol, x-axis precision, y-axis precision) are (blue diamond, 0.52 nm, 0.48 nm), (green cross, 0.33 nm, 0.33 nm) and (yellow circle, 0.50 nm, 0.64 nm). Scale bars, **a**, 3 nm; **b**, **c**, 15 nm; **d**, **e**, 200 nm; **f**, **g**, **h**, **i**, 20 nm.

photons may be collected indefinitely, to radically improve localization accuracies<sup>1</sup>.

The high-precision localization is apparent in a 2D map of the localizations from more than 400 INPALM frames on a single ANP (Fig. 5a). Almost  $10^8$  total photons were collected from the ANP without signs of degradation, averaging nearly 200,000 per frame. This enables calculation of localization accuracies of 0.76 Å and 0.50 Å in the long and short axis, respectively (Fig. 5c, Methods, Supplementary Discussion on localization analysis of single ANPs and Supplementary Tables 4 and 5).

To further demonstrate INPALM, we acquired diffraction-limited images of photoactivated ANPs from a sample containing a single 26/4 nm core–shell 8% Tm³+ ANP and an ANP trimer (Fig. 5d,e). Far-field optical and scanning electron microscopy (SEM) images show that

individual ANPs in the trimer cannot be resolved optically under wide-field illumination or with confocal scanning, even with the approximately 70 nm resolution possible due to the extreme nonlinearity of ANPs<sup>20</sup>. For each INPALM frame, ANP image spots were fit to a 2D Gaussian function, yielding a mean position and the standard error of that mean. This localization accuracy scales inversely with the square root of the number of collected photons (Fig. 5c,i). After each frame acquisition, the active ANPs within the region of interest are photodarkened and then a photobrightening beam is briefly applied to activate another random subset of ANPs within the same region. After repeated photoswitching cycles, a composite superresolution image is generated by first overlaying the centroid positions from each frame, then clustering the localizations using a Gaussian mixture method (Methods) and finally fitting the centroid position maps to a 2D Gaussian function.

This final fit provides the overall INPALM centroid positions for each ANP and their respective localization accuracies. Because an unlimited number of photodarkening-photobrightening cycles can be acquired without photodegradation, as many photons can be collected for each ANP as desired, leading to exceptionally precise localization accuracies. Corrections for sample drift and rotation are performed by imaging reference ANPs outside the region of interest, which remain active in each frame (Methods and Extended Data Fig. 10).

Because our ANPs are reasonably symmetrical (Fig. 1e), we observe that the localization centroid fittings are very close to the centres of ANPs determined by electron microscopy, within experimental limits (Fig. 5e). As with most superresolution imaging techniques, there is a tradeoff between imaging speed and localization accuracy, which depends on the number of photons collected (Supplementary Discussion). While the INPALM experiments in Fig. 5 were optimized for high localization accuracy, faster frame rates are also possible, down to 15 ms exposure time for photobrightening of 34% of ANPs (Extended Data Fig. 7d,  $I_{\text{ex},700 \,\text{nm}} = 240 \,\text{kW cm}^{-2}$ , 700 nm). Additionally, 91% of ANPs are turned off with an exposure time of 188 ms ( $I_{ex.1.064 \text{ nm}} = 252 \text{ kW cm}^{-2}$ , 1,064 nm). For signal acquisition times, under the conditions of Fig. 5, the average number of detected photons for a single ANP is approximately 50,000 counts for 500 ms (similar to signal levels for fluorescent proteins in reported PALM experiments<sup>27</sup>), which enables localization accuracy of a few nanometres per frame (Fig. 5a,f). Better accuracy can then be achieved by collecting from the same particle for multiple frames.

In conclusion, we report unlimited NIR photoswitching in inorganic ANPs, showing that they are photodarkened under NIR-II irradiation and recover with NIR-I or visible irradiation. We find no measurable degradation of ANP emission over more than 1000 repeated photoswitching cycles, under both ambient and aqueous conditions. The key mechanism of photoswitching in ANPs is revealed to be a discrete shift of PA threshold intensity mediated by defect-based colour centres in the core or at the core—shell interface. Further, we demonstrate superresolution imaging of ANPs with sub-Å localization precision, as well as rewritable 2D and 3D multihued optical patterning with modest NIR lasers. These results motivate the search for new ANP compositions demonstrating diverse photoswitching parameters<sup>53</sup> and open new pathways in a variety of applications including superresolution imaging<sup>4,24</sup>, high-density optical memory<sup>1,6,54,55</sup> and robust patterning in both two and three dimensions<sup>51,56</sup>.

#### **Online content**

Any methods, additional references, Nature Portfolio reporting summaries, source data, extended data, supplementary information, acknowledgements, peer review information; details of author contributions and competing interests; and statements of data and code availability are available at https://doi.org/10.1038/s41586-023-06076-7.

- Moerner, W. E. Single-molecule spectroscopy, imaging, and photocontrol: foundations for super-resolution microscopy (Nobel lecture). Angew. Chem. Int. Edn 54, 8067–8093 (2015).
- Keller, J., Schönle, A. & Hell, S. W. Efficient fluorescence inhibition patterns for RESOLFT microscopy. Opt. Express 15, 3361–3371 (2007).
- Heilemann, M. et al. Subdiffraction-resolution fluorescence imaging with conventional fluorescent probes. Angew. Chem. Int. Edn 47, 6172–6176 (2008).
- Dempsey, G. T., Vaughan, J. C., Chen, K. H., Bates, M. & Zhuang, X. Evaluation of fluorophores for optimal performance in localization-based super-resolution imaging Nat. Methods 8, 1027 (2011).
- Hou, L. et al. Optically switchable organic light-emitting transistors. Nat. Nanotechnol. 14, 347–353 (2019).
- Gu, M., Zhang, Q. & Lamon, S. Nanomaterials for optical data storage. Nat. Rev. Mater. 1, 16070 (2016).
- Dhomkar, S., Henshaw, J., Jayakumar, H. & Meriles, C. A. Long-term data storage in diamond. Sci. Adv. 2, e1600911 (2016).
- Velema, W. A., Szymanski, W. & Feringa, B. L. Photopharmacology: beyond proof of principle. J. Am. Chem. Soc. 136, 2178–2191 (2014).

- Molnár, G., Rat, S., Salmon, L., Nicolazzi, W. & Bousseksou, A. Spin crossover nanomaterials: from fundamental concepts to devices. Adv. Mater. 30, 1703862 (2018).
- Barber, P., Paschotta, R., Tropper, A. & Hanna, D. Infrared-induced photodarkening in Tm-doped fluoride fibers. Opt. Lett. 20, 2195–2197 (1995).
- Laperle, P., Chandonnet, A. & Vallée, R. Photoinduced absorption in thulium-doped ZBLAN fibers. Opt. Lett. 20, 2484–2486 (1995).
- Booth, I. J., Archambault, J.-L. & Ventrudo, B. F. Photodegradation of near-infrared-pumped Tm <sup>3+</sup>-doped ZBLAN fiber upconversion lasers. Opt. Lett. 21, 348–350 (1996).
- Sun, T., Su, X., Zhang, Y., Zhang, H. & Zheng, Y. Progress and summary of photodarkening in rare earth doped fiber. Appl. Sci. 11, 10386 (2021).
- Qin, G. et al. Photodegradation and photocuring in the operation of a blue upconversion fiber laser. J. App. Phys 97, 126108 (2005).
- Hu, Y. et al. X-ray-excited super-long green persistent luminescence from Tb3+ monodoped β-NaYF4. J. Phys. Chem. C 124, 24940–24948 (2020).
- Ou, X. et al. High-resolution X-ray luminescence extension imaging. Nature 590, 410–415 (2021).
- Wu, S. et al. Non-blinking and photostable upconverted luminescence from single lanthanide-doped nanocrystals. Proc. Natl Acad. Sci. USA 106, 10917-10921 (2009).
- Chan, E. M., Levy, E. S. & Cohen, B. E. Rationally designed energy transfer in upconverting nanoparticles. Adv. Mater. 27, 5753–5761 (2015).
- Wen, S. et al. Future and challenges for hybrid upconversion nanosystems. Nat. Photon. 13, 828–838 (2019).
- Lee, C. et al. Giant nonlinear optical responses from photon-avalanching nanoparticles. Nature 589, 230–235 (2021).
- Berkovic, G., Krongauz, V. & Weiss, V. Spiropyrans and spirooxazines for memories and switches. Chem. Rev. 100, 1741–1754 (2000).
- 22. Irie, M. Diarylethenes for memories and switches. Chem. Rev. 100, 1685-1716 (2000).
- Lukinavičius, G. et al. A near-infrared fluorophore for live-cell super-resolution microscopy of cellular proteins. Nat. Chem. 5, 132–139 (2013).
- Chozinski, T. J., Gagnon, L. A. & Vaughan, J. C. Twinkle, twinkle little star: photoswitchable fluorophores for super-resolution imaging. FEBS Lett. 588, 3603–3612 (2014).
- Beharry, A. A. & Woolley, G. A. Azobenzene photoswitches for biomolecules. Chem. Soc. Rev. 40, 4422–4437 (2011).
- Dickson, R. M., Cubitt, A. B., Tsien, R. Y. & Moerner, W. E. On/off blinking and switching behaviour of single molecules of green fluorescent protein. *Nature* 388, 355–358 (1997).
- Brakemann, T. et al. A reversibly photoswitchable GFP-like protein with fluorescence excitation decoupled from switching. Nat. Biotechnol. 29, 942–947 (2011).
- Erno, Z., Yildiz, I., Gorodetsky, B., Raymo, F. M. & Branda, N. R. Optical control of quantum dot luminescence via photoisomerization of a surface-coordinated, cationic dithienylethene. *Photochem. Photobiol. Sci.* 9, 249–253 (2010).
- Park, Y. I. et al. Nonblinking and nonbleaching upconverting nanoparticles as an optical imaging nanoprobe and T1 magnetic resonance imaging contrast agent. Adv. Mater. 21, 4467–4471 (2009).
- Nam, S. H. et al. Long-term real-time tracking of lanthanide ion doped upconverting nanoparticles in living cells. *Angew. Chem. Int. Edn* 50, 6093–6097 (2011).
- Gargas, D. J. et al. Engineering bright sub-10-nm upconverting nanocrystals for singlemolecule imaging. Nat. Nanotechnol. 9, 300–305 (2014).
- Fernandez-Bravo, A. et al. Continuous-wave upconverting nanoparticle microlasers. Nat. Nanotechnol. 13, 572–577 (2018).
- Fernandez-Bravo, A. et al. Ultralow-threshold, continuous-wave upconverting lasing from subwavelength plasmons. Nat. Mater. 18, 1172–1176 (2019).
- Akhmetov, S., Akhmetova, G., Kolodiev, B. & Samojlovich, M. Optical absorbtion spectra of YAG (Eu 2+, Eu 3+) and YAG (Yb 2+, Yb 3+) crystals. Zhurnal Prikladnoj Spektroskopii 48, 681–683 (1988).
- Broer, M., Krol, D. & DiGiovanni, D. Highly nonlinear near-resonant photodarkening in a thulium-doped aluminosilicate glass fiber. Opt. Lett. 18, 799–801 (1993).
- Engholm, M. & Norin, L. Preventing photodarkening in ytterbium-doped high power fiber lasers; correlation to the UV-transparency of the core glass. Opt. Express 16, 1260–1268 (2008).
- Lupi, J.-F. et al. Steady photodarkening of thulium alumino-silicate fibers pumped at 1.07 µm: quantitative effect of lanthanum, cerium, and thulium. Opt. Lett. 41, 2771–2774 (2016).
- Qin, X. et al. Suppression of defect-induced quenching via chemical potential tuning: a theoretical solution for enhancing lanthanide luminescence. J. Phys. Chem. C 123, 11151–11161 (2019).
- Zhuang, Y. et al. X-ray-charged bright persistent luminescence in NaYF4: Ln3+@ NaYF4
  nanoparticles for multidimensional optical information storage. *Light Sci. Appl.* 10, 132
  (2021).
- Bednarkiewicz, A., Chan, E. M., Kotulska, A., Marciniak, L. & Prorok, K. Photon avalanche in lanthanide doped nanoparticles for biomedical applications: super-resolution imaging. Nanoscale Horiz 4, 881–889 (2019)
- Liang, Y. et al. Migrating photon avalanche in different emitters at the nanoscale enables 46th-order optical nonlinearity. Nat. Nanotechnol. 17, 524–530 (2022).
- Kwock, K. W. et al. Surface-sensitive photon avalanche behavior revealed by singleavalanching-nanoparticle imaging. J. Phys. Chem. C 125, 23976–23982 (2021).
- Levy, E. S. et al. Energy-looping nanoparticles: harnessing excited-state absorption for deep-tissue imaging. ACS Nano 10, 8423–8433 (2016).
- Tian, B. et al. Low irradiance multiphoton imaging with alloyed lanthanide nanocrystals. Nat. Commun. 9, 3082 (2018).
- Kim, J. et al. Universal emission characteristics of upconverting nanoparticles revealed by single-particle spectroscopy. ACS Nano17, 648-656 (2022).
- Wang, F. et al. Simultaneous phase and size control of upconversion nanocrystals through lanthanide doping. Nature 463, 1061-1065 (2010).
- Narasimha Reddy, K. & Subba Rao, U. High-temperature X-ray irradiation induced thermoluminescence and half-life calculations in NaYF4 polycrystalline samples. Cryst. Res. Technol. 19, 1399–1403 (1984).

- Pedroso, C. C. et al. Immunotargeting of nanocrystals by SpyCatcher conjugation of engineered antibodies. ACS Nano 15, 18374–18384 (2021).
- Grotjohann, T. et al. Diffraction-unlimited all-optical imaging and writing with a photochromic GFP. Nature 478, 204–208 (2011).
- Barad, H.-N., Kwon, H., Alarcón-Correa, M. & Fischer, P. Large area patterning of nanoparticles and nanostructures: current status and future prospects. ACS Nano 15, 5861–5875 (2021).
- Hu, Z. et al. Reversible 3D optical data storage and information encryption in photo-modulated transparent glass medium. Light: Science & Applications 10, 140 (2021).
- Betzig, E. et al. Imaging intracellular fluorescent proteins at nanometer resolution. Science 313, 1642–1645 (2006).
- Zhang, Z. et al. Tuning phonon energies in lanthanide-doped potassium lead halide nanocrystals for enhanced nonlinearity and upconversion. *Angew. Chem. Int. Edn* 135, e202212549 (2022).
- Adam, V. et al. Data storage based on photochromic and photoconvertible fluorescent proteins. J. Biotechnol. 149, 289–298 (2010).

- Xie, N.-H. et al. Deciphering erasing/writing/reading of near-infrared fluorophore for nonvolatile optical memory. ACS Appl. Mater. Interfaces 11, 23750–23756 (2019).
- Zhuang, Y., Wang, L., Lv, Y., Zhou, T. L. & Xie, R. J. Optical data storage and multicolor emission readout on flexible films using deep-trap persistent luminescence materials. Adv. Funct. Mater. 28, 1705769 (2018).

**Publisher's note** Springer Nature remains neutral with regard to jurisdictional claims in published maps and institutional affiliations.

Springer Nature or its licensor (e.g. a society or other partner) holds exclusive rights to this article under a publishing agreement with the author(s) or other rightsholder(s); author self-archiving of the accepted manuscript version of this article is solely governed by the terms of such publishing agreement and applicable law.

© The Author(s), under exclusive licence to Springer Nature Limited 2023

#### **Methods**

#### **Materials**

Sodium trifluoroacetate (Na-TFA, 98%), sodium oleate, ammonium fluoride (NH<sub>4</sub>F), yttrium chloride (yCl<sub>3</sub>, anhydrous, 99.99%), thulium chloride (TmCl<sub>3</sub>, anhydrous, 99.9+%), gadolinium chloride (GdCl<sub>3</sub>, anhydrous, 99.99%), yttrium trifluoroacetate (99.99+%), oleic acid (OA, 90%) and 1-octadecene (ODE, 90%) were purchased from Sigma-Aldrich.

#### Synthesis of core and core-shell ANPs

NaY $_{1\cdot x}$ Tm $_x$ F $_4$ ANP cores with average diameters ranging from d = 10 nm to 18 ± 1 nm (Supplementary Table 1) were synthesized based on reported procedures $^{43,44}$ . For x = 0.01 (that is, 1% Tm $^{3+}$  doping), TmCl $_3$  (0.01 mmol, 2.8 mg) and yCl $_3$  (0.99 mmol, 193.3 mg) were added into a 50 ml three-neck flask following injection of 6 ml of OA and 14 ml of ODE. The mixture was stirred under vacuum and heated to 100 °C for 1h. The solution was pumped with vacuum and purged with N $_2$  over three cycles to remove water and oxygen. Subsequently, NH $_4$ F (4 mmol, 148 mg) and sodium oleate (2.5 mmol, 762 mg) were added to the flask with N $_2$  gas flow. Afterwards, the flask was resealed and placed under vacuum for 15 min at 100 °C, followed by analogous three cycles of alternating vacuum pump and N $_2$  purge for an additional 10 min. After that, the solution was quickly heated to 320 °C (with approximate ramp rate 25 °C min $^{-1}$ ). The temperature stayed at 320 °C for 40–60 min. The solution was cooled to room temperature with compressed air.

Ethanol was added to a tube containing the ANPs and the nanocrystals were separated by centrifugation for 5 min at 4,000 rpm. The dispersion with suspended pellets was additionally centrifuged to remove large aggregated particles. The nanoparticles were purified by a combination of ethanol wash, centrifuging and pellet dissolution in hexane. The whole cycle was repeated once more to further purify the nanocrystals. The nanocrystals were stored in hexane with two drops of OA to prevent aggregation.

#### **Shell growth**

A 0.1 M stock solution of 20% GdCl<sub>3</sub> and 80% YCl<sub>3</sub> was prepared by mixing YCl<sub>3</sub> (2 mmol, 390.5 mg), GdCl<sub>3</sub> (0.5 mmol, 131.8 mg), 10 ml OA and 15 ml ODE in a 50 ml three-neck flask. Gd<sup>3+</sup> was added to facilitate homogeneous shell growth<sup>46</sup>. The mixture was stirred under vacuum and heated to 110 °C for 30 min. The flask was filled with N<sub>2</sub> gas and heated to 200 °C for about 1 h, until the solution became clear and no solid was seen in the solution. The solution was cooled to 100 °C and placed under vacuum for 30 min. A 0.2 M solution of Na-TFA was prepared by mixing Na-TFA (4 mmol, 544 mg), 10 ml OA and 10 ml ODE in a flask, under vacuum, at room temperature for 2 h to ensure that all chemicals were dissolved. Then, 3–9 nm NaY<sub>0.8</sub>Gd<sub>0.2</sub>F4 shells (Supplementary Table 1) were grown on ANP cores using a layer-by-layer protocol<sup>57</sup> inside a nitrogen-filled glove box containing a workstation for automated nanocrystal discovery and analysis<sup>57</sup>. For example, for a 3 nm shell thickness, 6 ml ODE and 4 ml OA were injected to the dried ANP cores and heated to 280 °C at 20 °C per minute in the workstation for automated nanocrystal discovery and analysis glove box. A 0.2 M Na-TFA stock solution and a 0.1 M stock solution of 20% Gd and 80% Y oleate solution was added alternatively according to the automated protocols. Each alternating injection cycle was performed every 40 min (for example, one injection every 20 min) over six repeated cycles. After the last injection of each cycle, it was annealed at 280 °C for an additional 30 min. After that, it was cooled rapidly by N₂ gas flow. The core-shell particles were separated and purified using an identical purification protocol described above.

Core-shell NaYF $_4$  nanocrystals with varying Tm $^{3+}$  concentrations (from 1% to 100%) were fabricated using analogous protocols.

#### Nanoparticle characterization

TEM was achieved using a JEOL JEM-2100F field emission TEM operating at an acceleration voltage of 200 kV, FEI Themis 60-300 STEM/TEM

at an acceleration voltage of 300 kV and Tecnai T20 S-TWIN TEM at 200 kV with a LaB6 filament. The statistics of the nanocrystal sizes were calculated based on the size of approximately 100 nanoparticles using ImageJ software. X-ray diffraction (XRD) measurement was performed using a Bruker D8 Discover diffractometer with Cu K $\alpha$  radiation (Supplementary Figs. 1 and 2 and Supplementary Tables 1 and 2).

The high-resolution STEM images were acquired on an aberration corrected Titan 80–300 called TEAM 0.5 at the Molecular Foundry. The microscope was operated at 200 kV with a convergence semi-angle of 17 mrad and approximately 5 pA beam current. The 4D Camera was used to acquire a series of diffraction patterns from a grid of 1,024  $\times$  1,024 probe positions with real-space step size of 40 pm and acquisition time of 11  $\mu s$ . The centre of mass of each diffraction pattern was calculated and then used to estimate the phase of the electron beam by the differential phase contrast technique. Each algorithm was implemented in the open source stempy package. The phase is much more sensitive to weakly scattering atoms such as fluorine compared with the Z-contrast of the annular dark-field signal. This allowed us to image the atomic structure of beam sensitive ANPs to confirm they do not contain large scale defects.

#### Preparation of nanocrystal film samples

To prepare film samples, nanocrystals in a 40  $\mu$ l suspension with a concentration of 1  $\mu$ M were either drop-casted or spin-coated on a coverslip. Atomic force microscopy measurements (Bruker Dimension AFM) were performed to measure the film thickness of the prepared films.

#### Optical characterization of ANPs

For confocal microscopy of ANPs, an inverted confocal microscope (Nikon, Eclipse Ti-S) fitted with a 3D (XYZ) nanoscanning piezo stage (Physik Instrumente, P-545.xR8S Plano) was used. Single particles deposited on glass coverslips were excited with a 1,064-nm continuous-wave diode laser (Thorlabs, M9-A64-0300). A 950 nm long-pass filter (Thorlabs, FELH 950) and 950 nm short-pass dichroic mirror (Thorlabs, DMSP 950) were placed on the excitation beam path to filter out all the wavelengths above 950 nm. An 850 nm short-pass filter (Thorlabs, FESH 850) and a 750 nm long-pass filter (Thorlabs, FELH 750) were used to selectively collect the 800 nm photons from the sample. A 1.49 numerical aperture (NA) ×100 immersion oil objective (Olympus) and a 0.95 NA ×100 air objective lens (Nikon) were used for the imaging of single ANPs and ANP ensembles, respectively. Emitted light was directed to an electron-multiplying charge-coupled device-equipped spectrometer (Princeton Instruments, ProEM: 1600<sup>2</sup> eXcelon 3) or a single-photon avalanche diode (Micro Photon Device, PDM series). A neutral density wheel with a continuously variable density (Newport, 100FS04DV.4) was synchronized with the collection system and automatically rotated by an Arduino-controlled rotator to perform power dependence measurements. A Thorlabs power meter (PM100D and S120VC) simultaneously recorded the approximate 10% of the laser power reflected by a glass coverslip. Average excitation power densities were estimated using measured laser powers on the sample plane converted by the recorded laser power by the power meter and using the area calculated from the FWHM of the imaged laser spot.

For measuring the photobrightening activity spectra, we used a reflective objective lens (Thorlabs, LMM40X-P01), which does not show notable chromatic aberration, and selected filters (Thorlabs, FESH700 and FESH750) to block residual light from the 800 nm pump source.

Where appropriate, the error bars in optical data plots were derived by performing four separate measurements on the same single ANP (for single-ANP measurements) or on different regions of an ensemble film. For photodarkening and photobrightening experiments with ensemble films, we move 3  $\mu m$  away from the previously measured position to select a spot that was not photodarkened.

#### Time-tagged time-resolved luminescence

For time-resolved luminescence experiments of emission wavelengths less than 1,000 nm, a time-correlated single-photon counting (TCSPC) device (Picoquant, Hydraharp 400) coupled to a single-photon avalanche diode was used to record the timing data of detected photons. Time-tagged-time-resolved (TTTR) luminescence of ANP ensembles was measured by detecting single photons and recording the arrival time relative to the beginning of the measurement.

#### Time-resolved luminescence from the Tm<sup>3+3</sup>F<sub>4</sub> state

To measure the luminescence decay lifetime of the <sup>3</sup>F<sub>4</sub> state, a 1,064-nm continuous-wave laser (Qphotonics, QLD-1064-500S) was focused onto an ANP film placed on an inverted optical microscope (Olympus, IX73). A 50:50 beam splitter (Thorlabs, BSW511R) and a reflective objective lens (Thorlabs, LMM40X-P01) were installed in the microscope. The laser passed through a 1,064 nm bandpass filter and a 1,326 nm short-pass filter (Semrock, FF01-1326/SP-25) on the excitation beam path to block laser bleeding above 1,400 nm. Both 1100-nm and 1,500-nm long-pass filters (Thorlabs, FELH1100 and FELH1500) and a bandpass filter with the centre frequency of 2,000 nm and the FWHM of 500 nm (Thorlabs, FB2000-500) were placed on the collection beam path to block the laser beam and collect luminescence above 1,750 nm. The photons were collected by a superconducting nanowire single-photon detector coupled with an optical fibre (Single Quantum, EOS CS, 1,550 nm detector and HI 1060 fibre). The superconducting nanowire single-photon detector was connected to a time-correlated single-photon counting device (Picoquant, Hydraharp 400) to measure time-resolved MIR luminescence of the <sup>3</sup>F<sub>4</sub>-<sup>3</sup>H<sub>6</sub> transition.

#### Photoswitching of ANP ensemble films with two lasers

To investigate the photoswitching properties of ANP ensembles, illumination at 1,064 nm and 400–920 nm from a 1,064-nm continuous-wave diode laser (Thorlabs, M9-A64-0300) and a Ti-sapphire pulsed laser (Coherent, Chameleon OPO Vis, 80 MHz) or a 532 nm continuous-wave laser (Coherent, Sapphire CDRH) was focused on the ANPs on the inverted confocal microscope. A 950 nm short-pass dichroic mirror (Thorlabs, DMSP950R) was placed in the excitation beam path to merge two laser beams for photodarkening and photobrightening. The alignment of two laser beams at the sample plane was confirmed by measuring the beam images on a CMOS camera (Amscope, MU503) installed on a side port of the inverted microscope. The timing of the two illuminations was programmed by Scopefoundry, a custom Python-based software, which controls the two dual-position sliders (Thorlabs, ELL6).

#### Correlative light and electron microscopy for INPALM

The single ANPs on a glass coverslip marked by a finder grid (Gilder Grids, G200F1-C3) were placed on an inverted microscope (Nikon, Eclipse Ti2000-U). Wide-field illumination from a 1,064-nm continuous-wave diode laser (3SP Technologies, 1064CHP) and focused illumination from a 532 nm continuous-wave laser (Cobolt, Samba 50 mW) were directed on the sample through a 1.4 NA ×50 immersion oil objective (Nikon, PLAN APO ×60). The two-colour illuminations were alternated using two stepper motors which opened and closed a beam block on the signal of an Arduino board controlled by a Python-based program (Scopefoundry). To shift from 1,064 nm illumination for imaging to that for photodarkening, the beam size of the wide-field illumination was changed using a motorized flipper (Newport, 8892-K-M) in which a plano-convex lens (Thorlabs, AC254-400) was mounted. The 1,064 nm excitation intensities for imaging and photodarkening were 33.8 kW cm<sup>-2</sup> and 267 kW cm<sup>-2</sup>, respectively. The 532 nm excitation intensity for photobrightening was 842 kW cm<sup>-2</sup>. The probability of the photobrightening occurrence is governed by the statistical distribution in Extended Data Fig. 5a. The exposure times for darkening

and brightening were set to 2 s and 8 s, respectively. The samples under 1,064 nm excitation were imaged by an electron-multiplying charge-coupled device camera (Andor, iXon DU-888D-C00-#BV). The EM gain and the exposure time of the camera were set to 300 s and 1 s, respectively. The scanning electron microscopy was performed using a 10 kV SEM (Carl Zeiss, SigmaHD) after the sample was coated with platinum for 120 s using a sputter coater (Cressington, 108).

#### **Data processing for INPALM**

To reconstruct and quantify INPALM images, the centroid of point spread functions was estimated using a 2D Gaussian fitting. Each ANP image spot within a frame was fit to a 2D Gaussian function, yielding a mean position and the standard error of that mean (the localization accuracy). These fittings were then performed for each frame and a composite image was then generated by overlaying their centroid positions. Sample drift and rotation result in a dispersion of the collection of centroids for each ANP within this composite (Extended Data Fig. 10b,c). For Fig. 5, correction for lateral and rotational drift was achieved by imaging, in addition to the photoswitched ANPs, six reference ANPs within each frame that are not photoswitched during INPALM frame collection (Extended Data Fig. 10a). Corrections based on the point spread functions centroid fits of these six ANPs yielded ANP centroid positions from all the frames that were tightly clustered within approximately 20 nm regions in the corrected composite image (Extended Data Fig. 10d). Each of these centroid clusters (see, for example, Fig. 5a,f) is then fit to a 2D Gaussian function (Fig. 5b,h)<sup>58</sup>, with each centroid weighted by the number of photons collected for its evaluation, which provided the overall INPALM positions and localization accuracies for each ANP.

For ANPs in nanoscale proximity to one another, data processing using a Gaussian mixture method was used to separate a mixture of localizations into several groups (Fig. 5f,g)<sup>59</sup>. Also, the near-uniform brightness of each ANP proved beneficial, allowing the use of a simple intensity filter to reject frames that include more than one brightened ANP within a cluster, eliminating another source of error (Extended Data Fig. 10f). In rare instances, more than one particle can partially photobrighten, resulting in erroneous position localization estimates.

When the ANPs are used, for example, as targeted markers of biomolecule position, the localization accuracies will also be limited by factors such as the size and stiffness of the nanoparticle surface passivation and linker<sup>60</sup>. For kinetic studies of biomolecule motion, tracking of positional changes is limited largely by the stiffness of the surface passivation and linker, which determine how faithfully probe motion tracks biomolecule motion<sup>61</sup>.

#### **Data availability**

All data generated or analysed during this study, which support the plots within this paper and other findings of this study, are included in this published article and its Supplementary Information. Source data are provided with this paper.

#### **Code availability**

The code for modelling the PA behaviour using the differential rate equations described in the Supplementary Information is freely available at https://github.com/nawhgnahc/Photon\_Avalanche\_DRE\_calculation.git.

- 57. Chan, E. M. et al. Combinatorial discovery of lanthanide-doped nanocrystals with spectrally pure upconverted emission. *Nano Lett.* **12**, 3839–3845 (2012).
- Cnossen, J. et al. Localization microscopy at doubled precision with patterned illumination. Nat. Methods 17, 59–63 (2020).
- Lemmer, M., Inkpen, M. S., Kornysheva, K., Long, N. J. & Albrecht, T. Unsupervised vector-based classification of single-molecule charge transport data. *Nat. Commun.* 7, 12922 (2016).

- Wichner, S. M. et al. Covalent protein labeling and improved single-molecule optical properties of aqueous CdSe/CdS quantum dots. ACS Nano 11, 6773–6781 (2017).
- 61. Sudhakar, S. et al. Germanium nanospheres for ultraresolution picotensiometry of kinesin motors. Science **371**, eabd9944 (2021).

Acknowledgements We thank L. J. Kaufman at Columbia University for her technical support and S. Kim at KRICT for performing the SEM imaging. P.J.S., Y.D.S., S.H.N. and C.L. acknowledge support from the Global Research Laboratory (GRL) Program through the National Research Foundation of Korea (NRF) funded by the Ministry of Science and ICT (no. 2016911815) and KRICT (KK2361-10). Work at the Molecular Foundry was supported by the Office of Science. Office of Basic Energy Sciences, of the US Department of Energy (DOE) under contract no. DE-ACO2-05CH11231. C.L., P.J.S., B.E.C. and E.M.C. thank the Defense Advanced Research Project Agency (DARPA) Enhanced Night Vision in Eyeglass Form (ENVision) program (no. HR00112220006) for supporting the infrared spectroscopic investigations. Infrared emitter lifetime measurements were supported by the National Science Foundation under grant no. DMR-2019444. E.Z.X. acknowledges support from the NSF Graduate Research Fellowship Program. K.W.C.K. acknowledges support from the DOE NNSA Laboratory Residency Graduate Fellowship program (no. DE-NA0003960). P.J.S. also acknowledges support from Programmable Quantum Materials, an Energy Frontier Research Center funded by the US DOE, Office of Science, Basic Energy Sciences (BES), under award DE-SC0019443. Work at UNIST (Y.D.S.) was supported by IBS-R019-D1 and 2022 UNIST Research Fund (1.220108.01). We acknowledge seed funding support from Columbia University's Research Initiatives in Science & Engineering competition, started in 2004 to trigger high-risk, high-reward and innovative collaborations in the basic sciences, engineering and medicine: www.columbia.edu/rise. This research used resources of the National Energy Research Scientific Computing Center, a DOE Office of Science User Facility supported by the Office of Science of the US Department of

Energy under contract DE-ACO2-05CH11231. We thank Gatan Inc. as well as P. Denes, A. Minor, J. Ciston, C. Ophus, J. Joseph and I. Johnson who contributed to the development of the 4D Camera. N.F.M. acknowledges support from the European Union's Horizon 2020 research and innovation program under the Marie Sklodowska-Curie grant agreement no. 893439, the Fulbright Scholarship Program, the Zuckerman-CHE STEM Leadership Program and the ISEF Foundation. B.U. acknowledges support by the National Science Foundation under grant no. CHE-2203510. S.D.P. and T.L. acknowledge funding by the German Research Foundation (DFG) through the Collaborative Research Center 1032, Project no. 201269156, A8.

**Author contributions** P.J.S., C.L., E.M.C., B.E.C. and Y.D.S. conceived of the study. Experimental measurements and associated analyses were conducted by C.L., E.Z.X., K.W.C.K., B.U., M.E.Z., Y.K., N.F.M., C.C.S.P., H.S.P., J.K., S.H.N., S.D.P., T.L., J.S.O., P.E. and E.M.C. Advanced nanoparticle synthesis and characterization was performed by Y.L., A.T., C.C.S.P., H.S.P., B.E.C. and E.M.C. Theoretical modelling and simulations of PA photophysics were carried out by C.L. and E.M.C. All authors contributed to the preparation of the manuscript.

Competing interests The authors declare no competing interests.

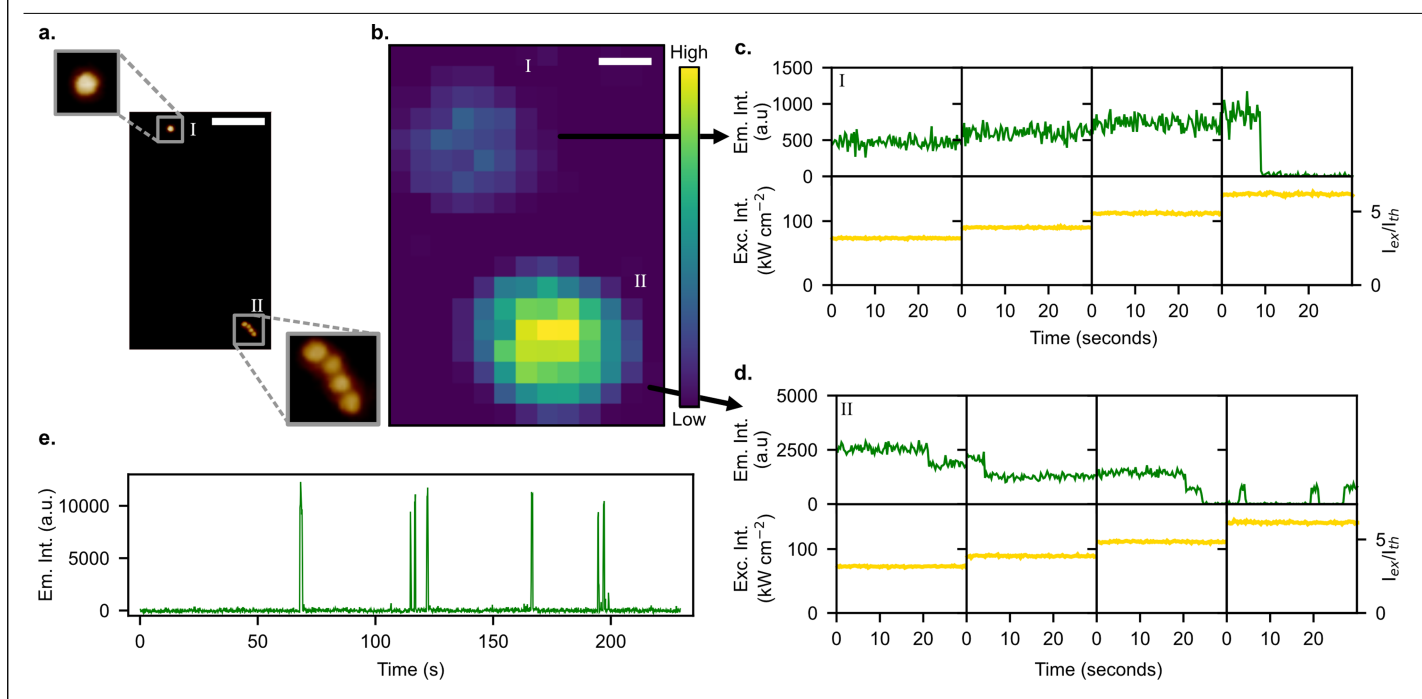
#### Additional information

 $\textbf{Supplementary information} \ The online version contains supplementary material available at \ https://doi.org/10.1038/s41586-023-06076-7.$ 

**Correspondence and requests for materials** should be addressed to Yung Doug Suh, Bruce E. Cohen, Emory M. Chan or P. James Schuck.

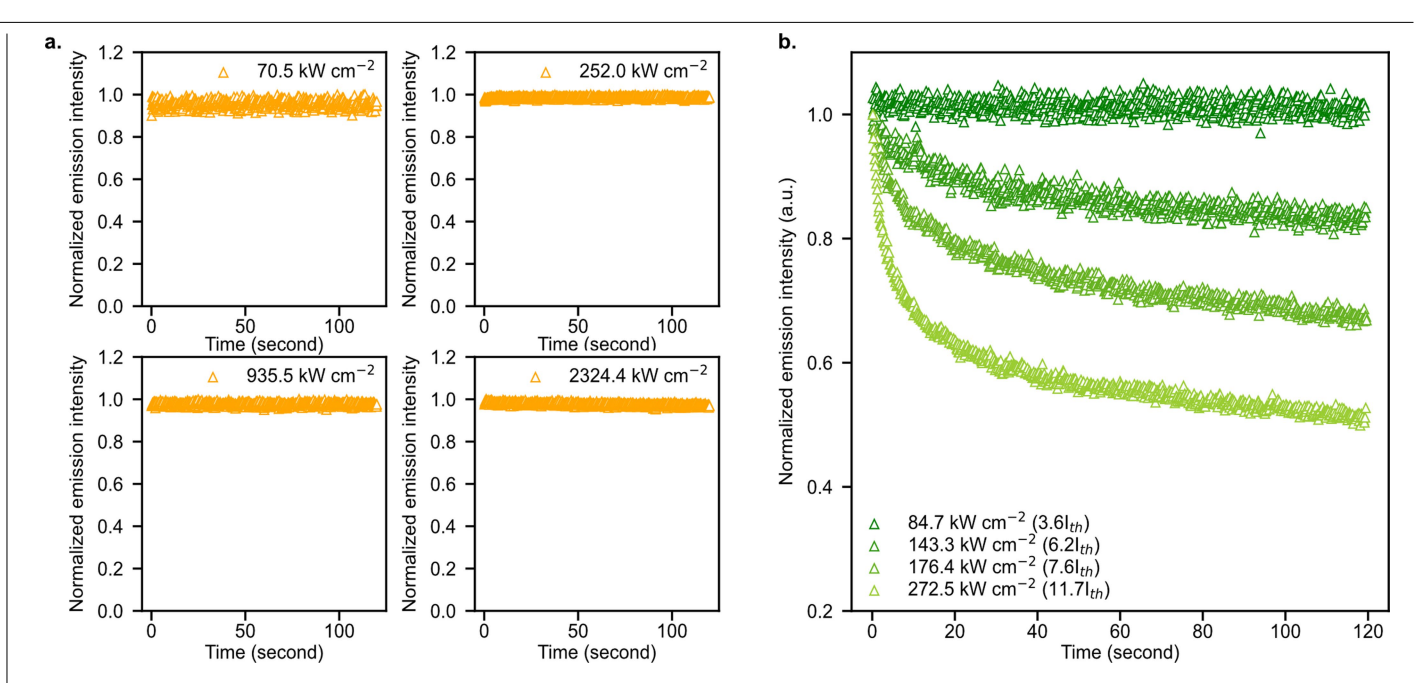
**Peer review information** *Nature* thanks Andries Meijerink and the other, anonymous, reviewer(s) for their contribution to the peer review of this work. Peer reviewer reports are available.

**Reprints and permissions information** is available at http://www.nature.com/reprints.



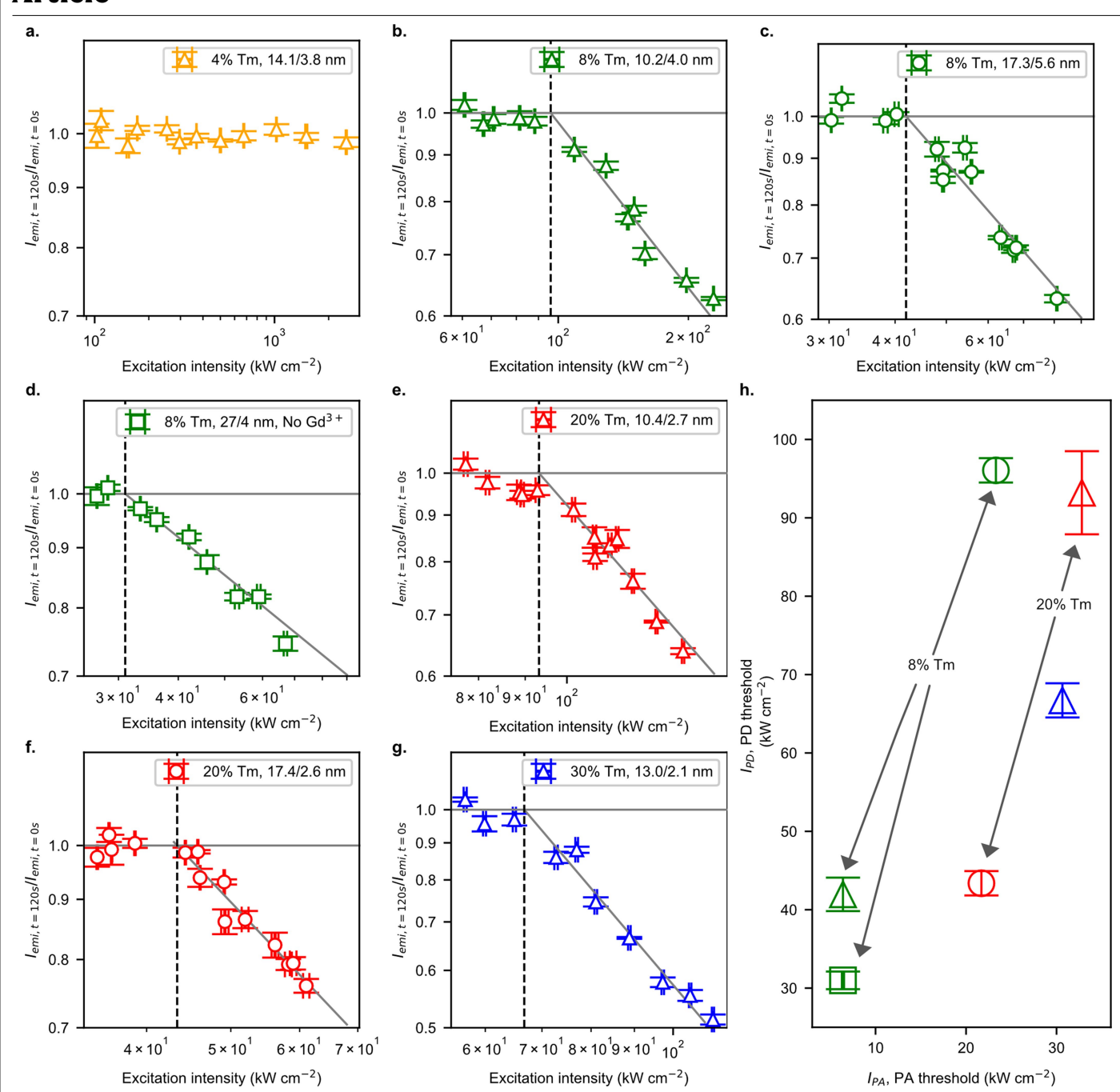
**Extended Data Fig. 1**| **Photodarkening and photoblinking in single ANPs.**(a) Atomic force microscopy (AFM) and (b) confocal scanning images of a single and a cluster of 4 ANPs (NaYF $_4$ : 8% Tm $^3$ \*@NaY $_{0.8}$ Gd $_{0.2}$ F $_4$ , 10 nm core/4 nm shell). Scale bars are 250 nm. Magnified AFM images of the ANPs are shown in the top left (single) and bottom right (4 singles) panels in a. Colour bar in b: normalized

luminescence intensity. Luminescence and excitation intensity  $l_{\rm ex}$  time-traces of the single  $(\boldsymbol{c})$  and four-ANP cluster  $(\boldsymbol{d})$  in  $\boldsymbol{a}$  under 1,064 nm excitation at increasing intensities.  $l_{\rm th}$ , ANP avalanching threshold intensity.  $\boldsymbol{e}$ , Time trace showing blinking luminescence from a single 8% Tm  $^{3*}$  17/6 nm core/shell nanocrystal at  $l_{\rm ex}$  = 164 kW cm  $^{-2}$ .



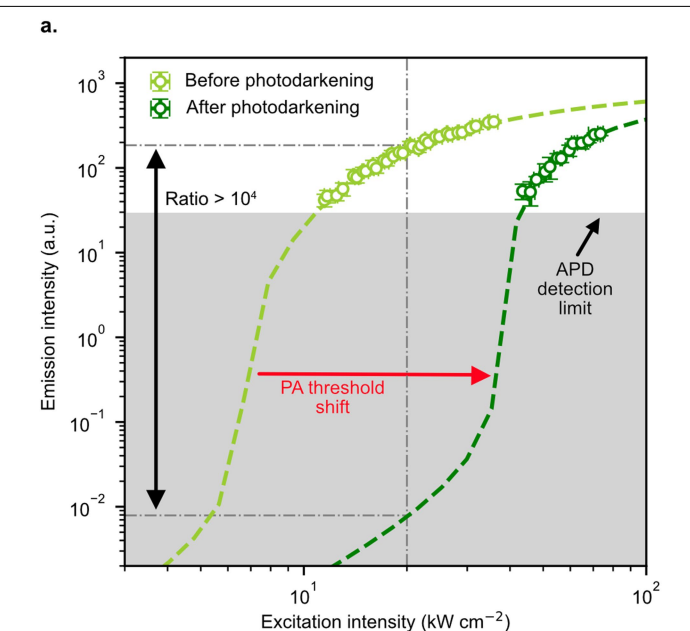
**Extended Data Fig. 2** | **Photodarkening in ANP ensembles. a**, Time dependence of 800 nm emission intensity at various 1064-nm excitation intensities, for 4% Tm<sup>3+</sup> 14.3/3.7 nm core/shell Tm<sup>3+</sup> nanoparticle ensemble films. UCNPs with Tm<sup>3+</sup>

doping  $\leq$  4% do not show avalanching behaviour 20, and photodarkening here. **b**, Time dependence of emission intensity at various 1,064-nm excitation intensity for 8% 10.2/4.0 nm core/shell Tm³+ ANP ensemble films.

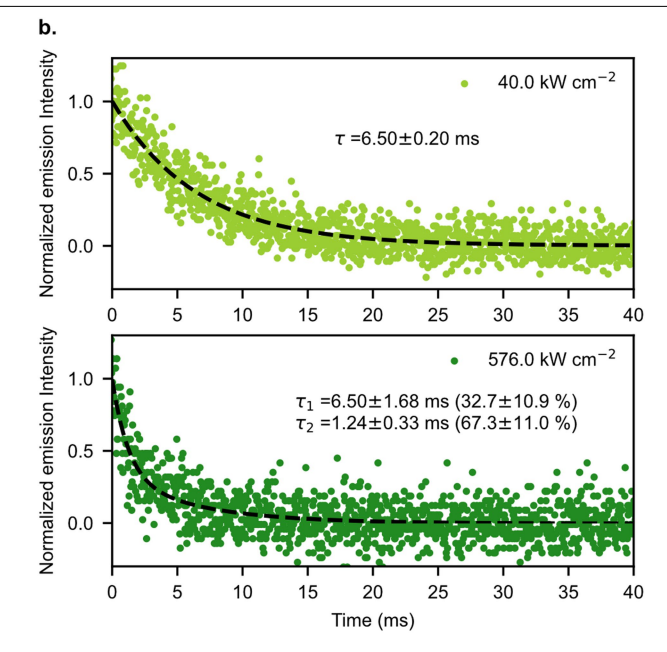


**Extended Data Fig. 3** | **Determination of photodarkening intensity**  $I_{PD}$  **as a function of ANP composition. a-g**, Each plot shows the ratio between 800 nm emission intensities ( $I_{emi}$ ) at t=0 and after 120 s of continuous 1,064 nm exposure versus excitation intensity. These data allow us to define a photodarkening threshold intensity ( $I_{PD}$ ) as the 1,064 nm pump intensity where emission at t=120 s decreases below the initial value. Error bars are standard

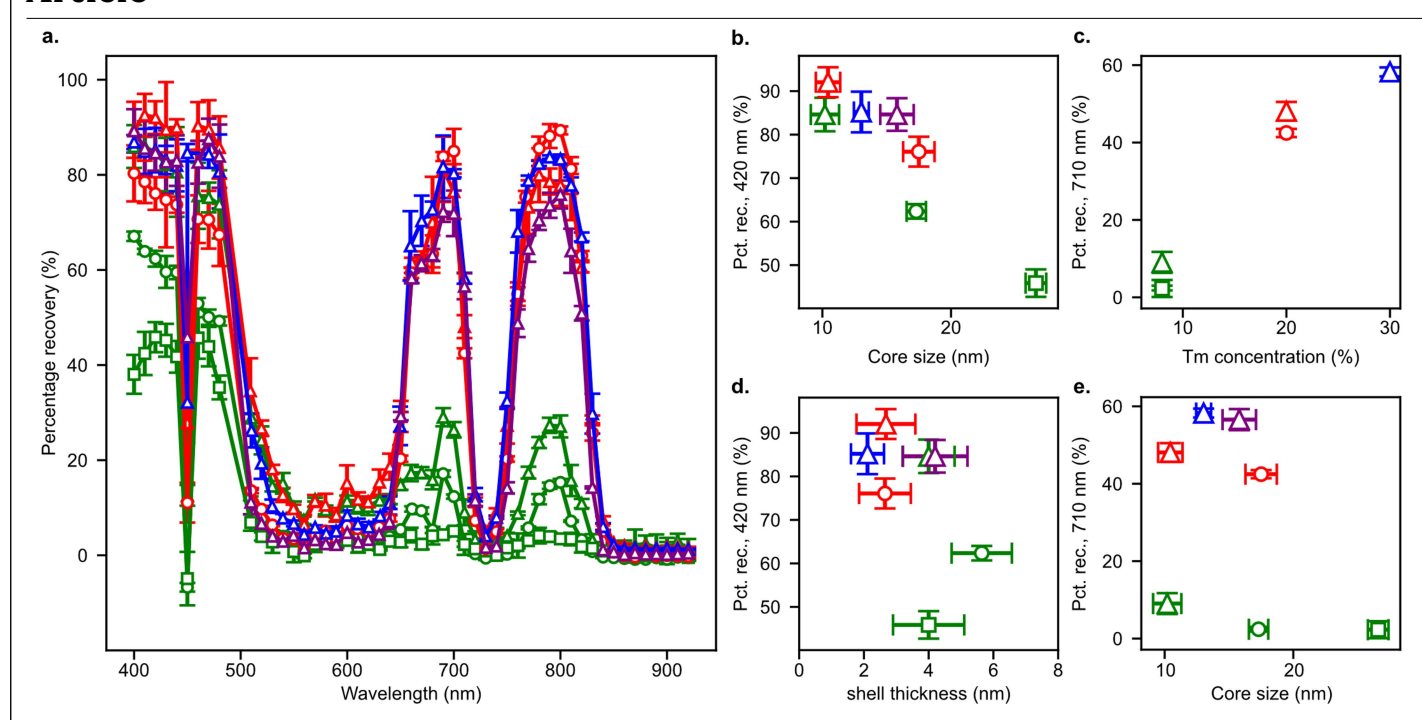
deviations of four data points measured at the same spot within 0.4 s. **h**, Photodarkening threshold versus pre-darkened photon avalanche threshold for various ANP compositions. Symbol definitions are the same as in  $\mathbf{a}-\mathbf{g}$ . Error bars are standard deviations derived from the curve fitting of the power-dependent photodarkening analysis shown in  $\mathbf{a}-\mathbf{g}$ .



# **Extended Data Fig. 4** | **PA threshold shift along with decrease of the** $^3F_4$ **lifetime. a**, Measurement (light and dark green circles) and differential rate equation model fitting (green dashed lines) of 800-nm emission intensity versus 1,064-nm excitation intensity of a single 17.3/5.6 nm 8% $^{3}Tm^{3+}$ (17 nm core with 5.6 nm shells) ANP before and after photodarkening. Error bars are standard deviations derived from four separate measurements on the same single ANP. **b**, Time-resolved photoluminescence of IR emission from the $^{3}Tm^{3+$

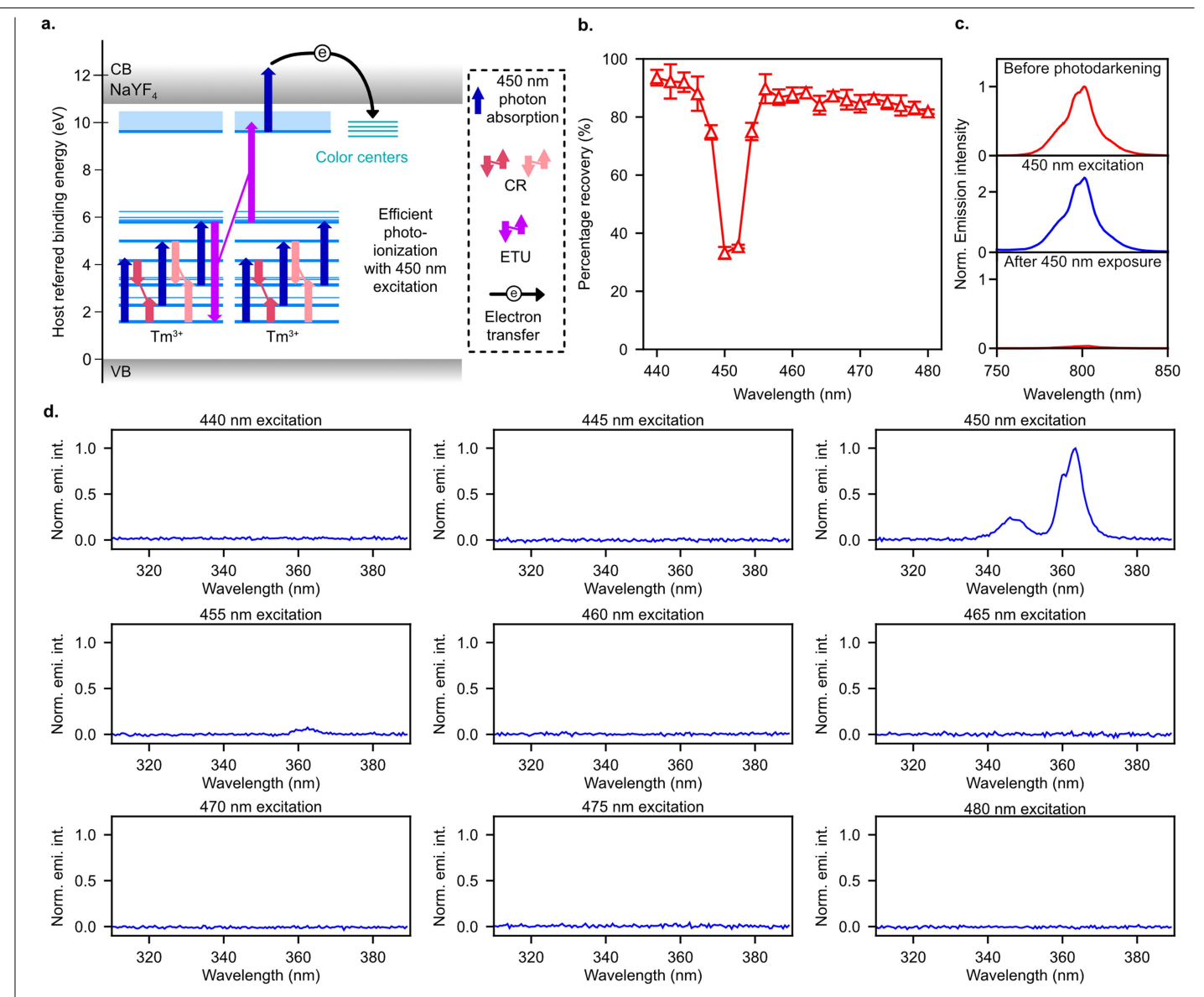


wavelengths >1,750 nm were selected with a long-pass filter and collected using a superconducting nanowire single-photon detector (SNSPD; Single Quantum EOS 6). A single exponential decay is observed in the non-photodarkened ANPs (top panel). The lifetime curve from the photodarkened region (bottom panel) includes contributions from non-photodarkened ANPs within the film, resulting in a biexponential decay. The biexponential decay analysis suggests approximately two thirds of the ANPs are photodarkened in the measureed region, and the photodarkend ANPs have a  $^3F_4$  lifetime that is 5.2 times shorter, consistent with the rate equation analysis and fits in Fig. 3a.



Extended Data Fig. 5 | Photobrightening recovery percentage of various ANP ensemble film samples. a, Photobrightening recovery of darkened ANP films as a function of irradiation wavelength. The  $Tm^{3+}$  contents for green, red, blue, and purple markers are 8%, 20%, 30%, and 100%. Excitation (1,064 nm) and photobrightening intensities are  $54~kW~cm^{-2}$  and  $277.87~kW~cm^{-2}$ , respectively, for green triangles (10.2/4 nm), red triangles (10.4/2.7), blue triangles (13.0/2.1 nm), and purple triangles (15.8/4.2 nm). Excitation (1,064 nm) and photobrightening intensities are  $33~kW~cm^{-2}$  and  $167~kW~cm^{-2}$ ,

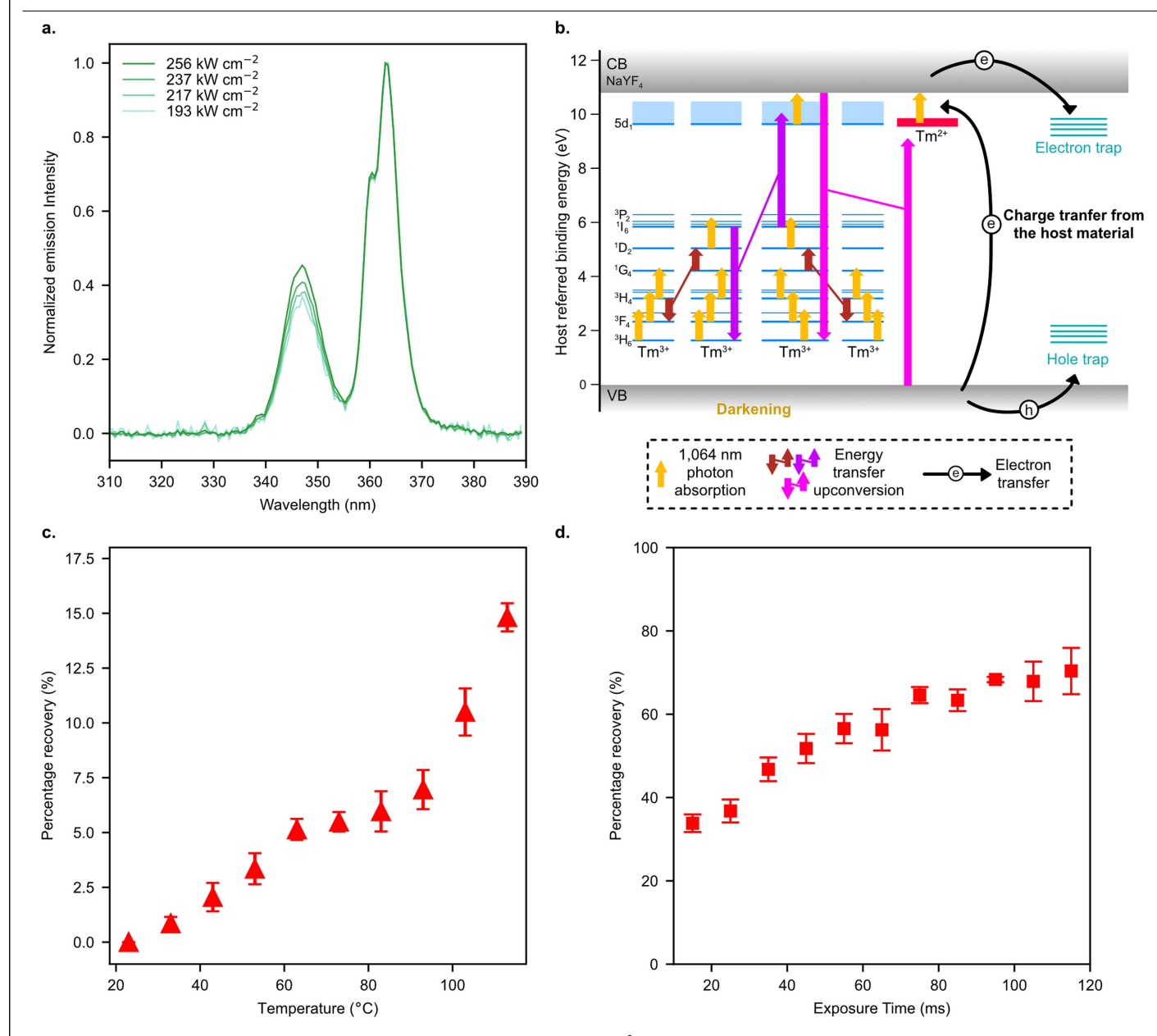
respectively, for green circles (17.3/5.6 nm), green squares (26.6/4.0 nm), and red circles (17.5/2.7 nm). Exposure times for photodarkening and photobrightening are 1.2 and 1.3 s, respectively. Error bars are standard deviations of data points measured at the four different spots in the same ensemble sample. The photobrightening laser power at the sample is set to 1 mW. Photobrightening recoveries as a function of ANP core size at 420 nm ( $\bf b$ ), Tm³+ concentration at 710 nm ( $\bf c$ ), shell thickness at 420 nm ( $\bf d$ ), and core size at 710 nm ( $\bf e$ ).



#### Extended Data Fig. 6 | ANP photodarkening with 450 nm excitation.

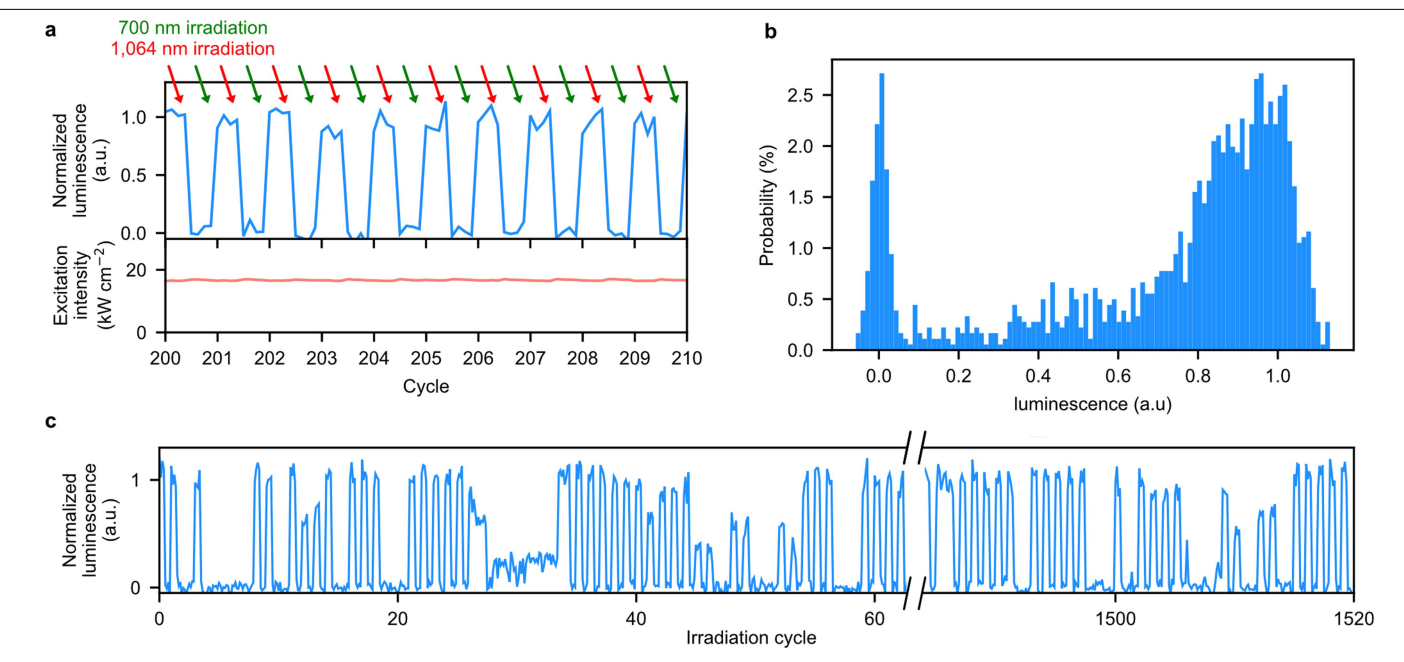
**a**, Potential mechanistic pathways for photodarkening in ANPs under 450 nm excitation. **b**, Photobrightening recovery of darkened 20% Tm $^{3+}$ 10.4/2.7 nm core diameter/shell thickness ANP films as a function of irradiation wavelength from 440 nm to 480 nm. The photobrightening laser power at the sample is set to 1 mW for all wavelengths. **c**, Emission spectra from an ensemble film of 20% Tm $^{3+}$ 10.4/2.7 nm core diameter/shell thickness ANPs before photodarkening (top), during 450 nm exposure (middle), and after photodarkening with 450 nm exposure (bottom).1,064 nm illumination is used for pumping the

luminescence in the left and right panels. The 1,064 nm intensity is 75 kW cm $^{-2}$ , and the 450 nm excitation intensity is 222 kW cm $^{-2}$ . The emission intensities in  $\boldsymbol{b}$  are normalized to the maximum intensity in the left panel.  $\boldsymbol{d}$ , UV emission spectra of 20% Tm $^{3*}$ 10.4/2.7 nm core diameter/shell thickness ANPs under blue excitation with a wavelength range from 440 nm to 480 nm. The excitation powers are 1 mW. The emission intensities in  $\boldsymbol{c}$  are normalized to the maximum intensity in the panel obtained under 450 nm excitation. The 345 nm and 365 nm emission peaks are attributed to the excited-state transitions from the  $^1I_6$  state to the  $^3F_4$  state and the  $^1D_2$  state to the  $^3H_6$  state, respectively.



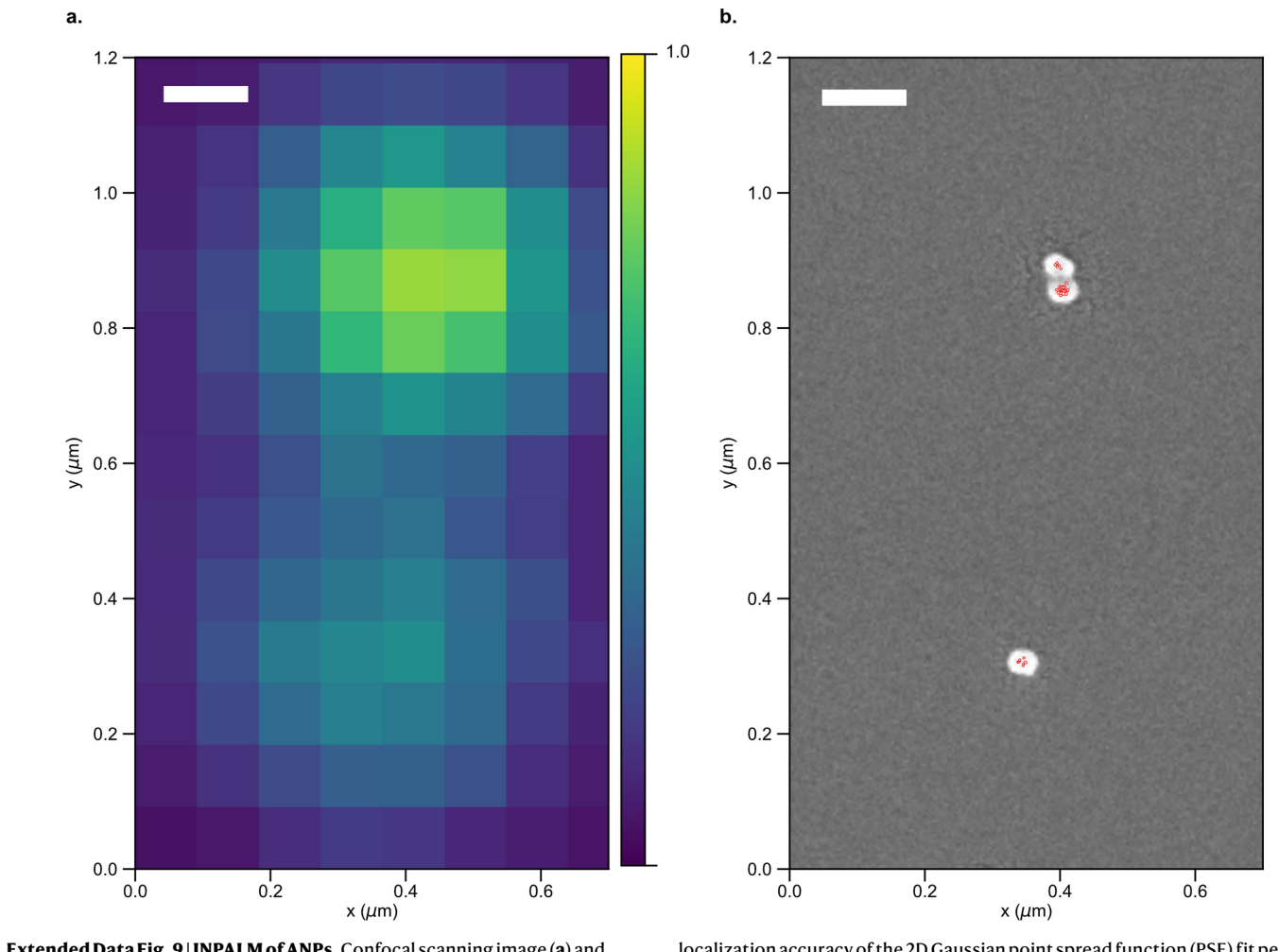
Extended Data Fig. 7 | Photodarkening and photobrightening mechanisms and fast photobrightening with sub-20-ms exposure. a, Ultraviolet emission spectra of 8% Tm³+ 17.3/5.6 nm ANP ensembles at 1,064-nm excitation intensities above photodarkening threshold intensity ( $I_{\rm PD}$ ). Spectra are normalized to the 365 nm peak. The 345 nm and 365 nm emission peaks are attributed to the excited-state transitions from  ${}^1I_6$  to  ${}^3F_4$  and  ${}^1D_2$  to  ${}^3H_6$ , respectively. **b**, Potential mechanistic pathways for photodarkening and photobrightening in ANPs via charge transfer from the host material, resulting in Tm²+ as an intermediate. CB: conduction band, VB: valence band,  $W_2$ :  ${}^3F_4$  relaxation rate. Hole traps in addition to electron traps can be produced through the charge transfer process, which can both potentially quench the  ${}^3F_4$  excited state in Tmions. **c**, Recovery was accomplished with external heating only (5 min equilibration at each temperature), rather than by photobrightening. Before and after heating, 20%

 $Tm^{3*}\,10.4/2.7\,nm$  films were photodarkened and probed with  $1064\,nm$  intensities of  $320\,kW\,cm\text{-}2$  and  $64\,kW\,cm\text{-}2$ , respectively. Percentage recovery is defined as the ratio of the recovered luminescence intensity after temperature increase to the reduced luminescence intensity after initial photodarkening. Error bars are standard deviations of data points measured at the four different spots in the same film.  $\boldsymbol{d}$ , Photodarkened regions of a film of  $20\%\,Tm^{3*}\,10.4/2.7\,nm$  core/shell ANPs were exposed to a 700 nm photobrightening beam for short exposure times, and the luminescence recovery was measured as a function of exposure time. The  $1064\,nm$  pumping and photodarkening intensities are  $51\,kW\,cm^{-2}$  and  $252\,kW\,cm^{-2}$ , respectively. 700 nm photobrightening excitation intensity is  $240\,kW\,cm^{-2}$ . The photodarkening exposure time is  $188\,ms$ . Error bars are standard deviations of data points measured at the four different spots in the same ensemble sample.



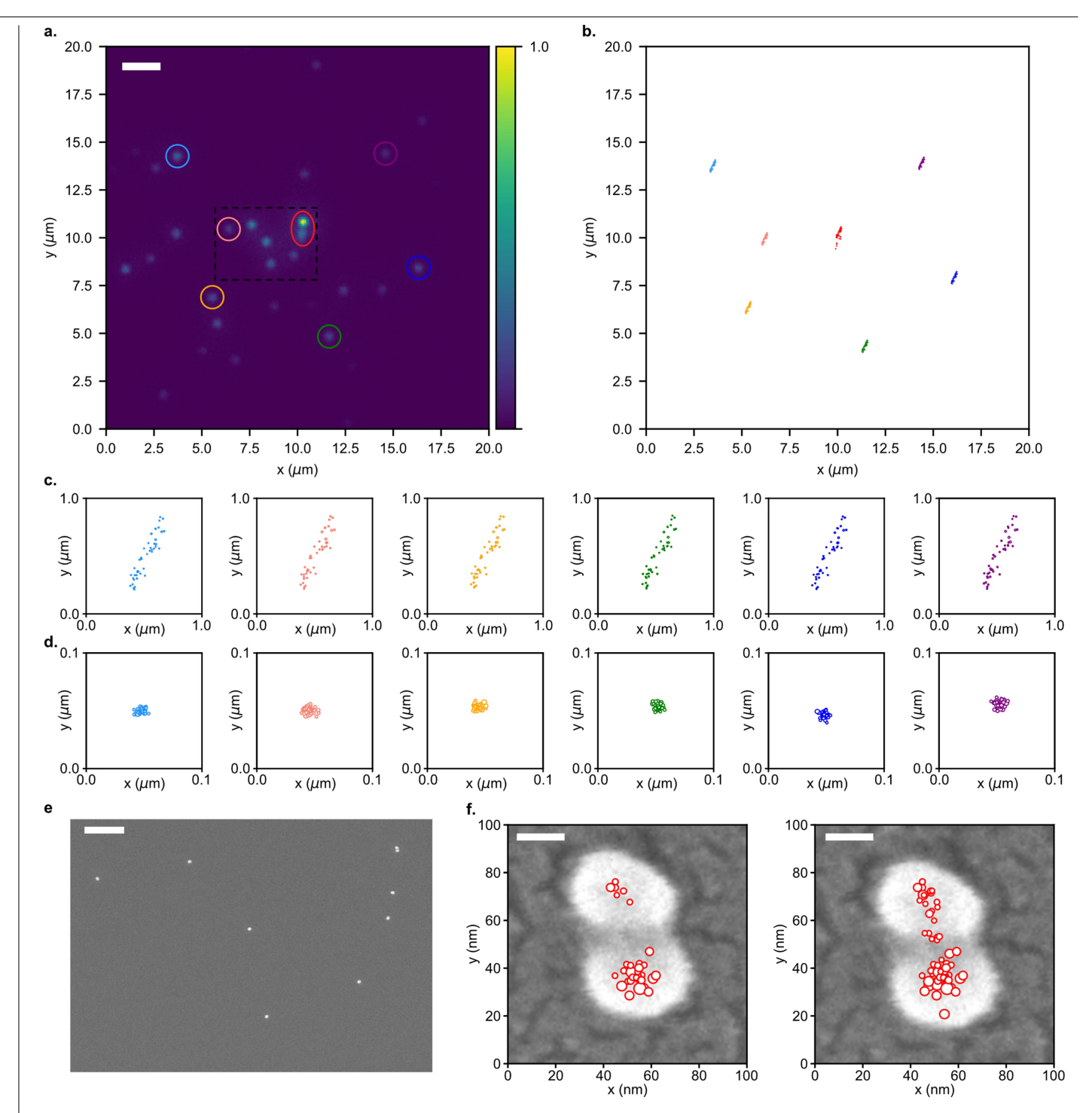
**Extended Data Fig. 8** | **Indefinite photoswitching of a single aqueous ANP. a**, Time-resolved luminescence and excitation intensities for a single 8% Tm $^{3+}$  17.3/5.6 nm aqueous ANP $^{48}$  in water . A1,064 nm pump intensity of 16.7 kW cm $^{-2}$  is continuously applied, which excites detectable emission in the on state but not in the off state. Irradiation conditions for photodarkening (turning off) are

 $75.5\,kW\,cm^{-2}$  at  $1,064\,nm$  and  $5\,s$ ; and for recovery (turning on) are  $164.0\,kW\,cm^{-2}$  at  $700\,nm$  for  $10\,s.$  b, A probability histogram of the average emission intensity while turning on for 1,520 irradiation cycles. c, Trace of emission from the single aqueous ANP for the first  $60\,and\,last$   $35\,irradiation$  cycles.



**Extended Data Fig. 9 | INPALM of ANPs.** Confocal scanning image (a) and INPALM image (b) (number of localizations, N=43) of a single and a dimer of 8% Tm $^{3+}$  26.6/3.0 nm ANPs. The diameter of the localization in **b** represents the

localization accuracy of the 2D Gaussian point spread function (PSF) fit per frame. Scale bars are 125 nm.



**Extended Data Fig. 10 | INPALM of ANPs with drift correction and intensity filtering. a**, Wide-field image of ANPs of 8% Tm $^{3+}$ 26.6/3.0 nm ANPs. Scale bar is  $2 \mu m$ . **b**, Frame-by-frame localizations of the ANPs marked with circles in **a** before drift correction. Only particles in the red circle (identical to the ANPs in Extended Data Fig. 9) are exposed to periodic 1,064 nm and 532 nm illumination for photoswitching. The other ANPs in the circles are in the on state while photoswitching the ANPs in the red circle and used for drift correction.

Magnified frame-by-frame localizations of the ANPs marked with circles in **a** before (**c**) and after drift correction (**d**). The diameter of the localization in **c** represent the 10 times of the standard deviation of the 2D Gaussian point spread function (PSF), and that in **d** represent the standard deviation of the 2D Gaussian PSF. **e**. SEM images of ANPs in a region marked with dashed lines in **a**. Scale bar is 500 nm. **f**, Frame-by-frame localizations of the ANPs marked with a red circle in **a** before (left) and after (right) intensity filtering.